

Testing the disk-corona interplay in radiatively-efficient broad-line AGN

R. Arcodia¹, A. Merloni¹, K. Nandra¹, and G. Ponti^{1,2}

¹ Max-Planck-Institut für Extraterrestrische Physik (MPE), Giessenbachstrasse 1, 85748 Garching bei München, Germany
e-mail: arcodia@mpe.mpg.de

² INAF-Osservatorio Astronomico di Brera, Via Bianchi 46, 23807 Merate, LC, Italy

Received 12 May 2019 / Accepted 18 July 2019

ABSTRACT

The correlation observed between monochromatic X-ray and UV luminosities in radiatively-efficient active galactic nuclei (AGN) lacks a clear theoretical explanation despite being used for many applications. Such a correlation, with its small intrinsic scatter and its slope that is smaller than unity in log space, represents the compelling evidence that a mechanism regulating the energetic interaction between the accretion disk and the X-ray corona must be in place. This ensures that going from fainter to brighter sources the coronal emission increases less than the disk emission. We discuss here a self-consistently coupled disk-corona model that can identify this regulating mechanism in terms of modified viscosity prescriptions in the accretion disk. The model predicts a lower fraction of accretion power dissipated in the corona for higher accretion states. We then present a quantitative observational test of the model using a reference sample of broad-line AGN and modeling the disk-corona emission for each source in the L_X-L_{UV} plane. We used the slope, normalization, and scatter of the observed relation to constrain the parameters of the theoretical model. For non-spinning black holes and static coronae, we find that the accretion prescriptions that match the observed slope of the L_X-L_{UV} relation produce X-rays that are too weak with respect to the normalization of the observed relation. Instead, considering moderately-outflowing Comptonizing coronae and/or a more realistic high-spinning black hole population significantly relax the tension between the strength of the observed and modeled X-ray emission, while also predicting very low intrinsic scatter in the L_X-L_{UV} relation. In particular, this latter scenario traces a known selection effect of flux-limited samples that preferentially select high-spinning, hence brighter, sources.

Key words. galaxies: nuclei – quasars: general – quasars: supermassive black holes – X-rays: general – accretion, accretion disks – galaxies: active

1. Introduction

The development of an in-depth understanding of accretion physics in active galactic nuclei (AGN) has tended to lag behind in comparison to other accreting objects (e.g., X-ray binaries, cataclysmic variables, and protoplanetary disks), for which many more observational constraints are available. While it seems that the standard thin-disk model (Shakura & Sunyaev 1973, hereafter *SS73*) is not able to fully explain the plethora of accreting sources that we observe (e.g., Koratkar & Blaes 1999; Blaes 2007; Antonucci 2015), it is still unclear to what extent this simple but effective prescription has to be improved (Kishimoto et al. 2008; Capellupo et al. 2015, 2016).

Since the first AGN X-ray spectral surveys were performed (e.g. Elvis et al. 1978; Turner & Pounds 1989), the need for an additional spectral component to extend the cold-disk's \lesssim keV temperatures was evident. This so-called X-ray “corona” (e.g. Liang & Price 1977; Galeev et al. 1979) is now almost universally considered as a hot ($\sim 10^9$ K), optically thin ($\tau \lesssim 1$) plasma up-scattering the disk photons via thermal Comptonization (Haardt & Maraschi 1991, 1993; Haardt et al. 1994; Stern et al. 1995), although an additional warm component is sometimes needed to fit the softest X-rays (Petrucci et al. 2018; Kubota & Done 2018, and references therein). The proximity of the corona to the central black hole was immediately suggested by its strong and fast variability (e.g. McHardy 1989) and by

the reflection signatures (Lightman & White 1988; Pounds et al. 1990; Nandra et al. 1991; Williams et al. 1992; Tanaka et al. 1995), but in-depth information regarding its geometry and formation mechanism is still lacking.

The geometry of the corona can be constrained via the observation of X-ray reverberation lags (Fabian et al. 2009, 2017; De Marco et al. 2013; Uttley et al. 2014), that seem to show a, possibly non-static, corona extending vertically and radially over the underlying disk for a few and a few tens of gravitational radii, respectively (Wilkins et al. 2016). The compactness of the corona and the origin of the X-rays close to the black hole also appear to be confirmed by micro-lensing results (e.g. Mosquera et al. 2013; Reis & Miller 2013).

As far as the formation of the corona is concerned from the theoretical point of view, the most likely explanation for it is that it is magnetically-dominated with an efficient saturation of the magnetic field that is amplified via the magneto-rotational instability (MRI, Chandrasekhar 1960; Balbus & Hawley 1991, 1992; Hawley & Balbus 1991, 1992) and extending buoyantly upward (and downward) from the denser parts of the disk (Galeev et al. 1979; Stella & Rosner 1984; Di Matteo 1998; Merloni & Fabian 2002; Blackman & Pessah 2009). Magnetic reconnection can then keep the corona hot (e.g., Liu et al. 2002; Uzdensky & Goodman 2008; Uzdensky 2016; Beloborodov 2017; Werner et al. 2019; Ripperda et al. 2019). This scenario seems to be supported by magneto-hydrodynamic (MHD)

simulations (Miller & Stone 2000; Uzdensky 2013; Bai & Stone 2013; Jiang et al. 2014; Salvesen et al. 2016; Kadowaki et al. 2018), although only qualitative comparisons with observations have been made so far (however, see Schnittman et al. 2013). Much effort has, nonetheless, been put into trying to shed light on the physics of the disk-corona system (see Blaes 2014) and this will continue with global 3D radiation-MHD simulations (e.g. Jiang et al. 2017a), that are now approaching sub-Eddington flows as well (Jiang et al. 2019).

Observationally, the increase in quality and quantity of available AGN X-ray-to-UV data from large samples can provide insightful, and more easily approachable, diagnostics. The smoking gun of the disk-corona interplay in radiatively efficient AGN is given by the non linear correlation observed between the 2 keV and 2500 Å monochromatic luminosities (e.g., Vignali et al. 2003; Strateva et al. 2005; Steffen et al. 2006; Young et al. 2009; Lusso et al. 2010; Lusso & Risaliti 2016, and references therein), that persists throughout the common observed X-ray and optical-UV bands (Jin et al. 2012). Despite the possible differences arising from different sample selections and regression techniques, most observations point towards a $\log L_X - \log L_{UV}$ correlation with a slope ≈ 0.6 , a dispersion that can be as small as $\sigma \approx 0.2$ dex (Lusso & Risaliti 2016; Chiaraluce et al. 2018), and no apparent redshift dependency. Such a tight correlation paved the way for quasars to provide an alternative standard candle for cosmographic studies (Risaliti & Lusso 2015, 2019). The slope, being smaller than unity, indicates that from lowly to highly accreting AGN, the disk emission increases more than the corona emission (e.g., Kelly et al. 2008) with crucial implications for the physics governing the coupled disk-corona system. However, a solid and conclusive theoretical explanation, for what is one of the most studied multi-wavelength observables in AGN, is still lacking.

The goal of this paper is indeed to test a self-consistently coupled disk-corona analytic model against the observed $L_X - L_{UV}$. Given the existing gap between simulations and observations, we argue that the use of simplified (but motivated) prescriptions still represents a powerful tool to explain observed disk-corona scaling relations, as it was done with the X-ray photon index (or the X-ray bolometric correction) correlation with the Eddington ratio (Wang et al. 2004, 2019; Cao 2009; Liu & Liu 2009; You et al. 2012; Liu et al. 2012, 2016a), or with the $\log L_X - \log L_{UV}$ itself (Lusso & Risaliti 2017, hereafter LR17; Kubota & Done 2018). We here rely uniquely on the $\log L_X - \log L_{UV}$ relation, since monochromatic L_X and L_{UV} values can be directly obtained from spectral fits. Forward modeling monochromatic luminosities circumvents difficulties and issues typical of model comparisons with accretion rate, Eddington ratio or bolometric luminosity estimates (e.g., Richards et al. 2006; Davis & Laor 2011; Slone & Netzer 2012; Krawczyk et al. 2013; Capellupo et al. 2015, 2016; Kilerci Eser & Vestergaard 2018).

We describe our disk-corona model in Sect. 2 (and Appendix A) and we briefly show its qualitative predictions in Sect. 3. Then, we outline the observational test that we put forward to thoroughly understand the disk-corona interplay in Sect. 4 and we show the results in Sect. 5. Throughout this work, we quote median values with 16th and 84th percentiles unless otherwise stated.

2. The disk-corona model

The disk-corona model adopted in this work is largely based on the prescriptions put forward by Merloni (2003, hereafter M03;

see also Merloni & Fabian 2002, 2003), in which the standard conservation equations of a geometrically-thin and optically-thick accretion disk (SS73; Pringle 1981) are self-consistently coupled with the X-ray corona, indicated as the fraction f (e.g., Haardt & Maraschi 1991; Svensson & Zdziarski 1994) of accretion power (per unit area, Q_+) that is dissipated away from the cold disk (e.g., Stella & Rosner 1984; Di Matteo 1998):

$$f = \frac{Q_{\text{cor}}}{Q_+} \quad (1)$$

with $Q_{\text{cor}} = v_D P_{\text{mag}}$ and $Q_+ = \frac{3}{2} c_s \tau_{r\phi}$, where v_D is the vertical drift velocity (taken proportional to the Alfvén speed via an order-unity constant b), $P_{\text{mag}} = B^2/8\pi$ is the magnetic pressure, c_s is the sound speed and $\tau_{r\phi}$ is the vertically-averaged stress tensor.

The stress tensor can be assumed to be dominated by Maxwell stresses (e.g., Hawley et al. 1995; Sano et al. 2004; Minoshima et al. 2015), from which we can write $\tau_{r\phi} = k_0 P_{\text{mag}}$, with k_0 being a constant of order unity (Hawley et al. 1995). To build a self-consistent solution to the accretion problem, we need to relate the stress tensor (via the magnetic pressure) with local quantities that standard analytic models are familiar with. As a matter of fact, the α -prescription is not the only educated guess that is adopted to dodge our ignorance of the physical mechanism producing the disk viscosity. Within the same theoretical framework, fundamental modifications to the viscosity law can be introduced depending on whether the viscous stress is assumed to scale proportionally with the total (P_{tot} , gas plus radiation) pressure (SS73), with the gas pressure alone (Lightman & Eardley 1974; Sakimoto & Coroniti 1981; Meyer & Meyer-Hofmeister 1982; Stella & Rosner 1984) or with the geometric mean of the two (M03; Ichimaru 1977; Taam & Lin 1984; Burm 1985). It was soon discovered that the first prescription leads to thermally and viscously unstable disks in the radiation-pressure dominated regions, with the first instability acting on shorter timescales (Lightman & Eardley 1974; Shakura & Sunyaev 1976; Pringle 1976). This encouraged many authors (Hoshi 1985; Szuszkiewicz 1990; Merloni & Nayakshin 2006; Grzędzielski et al. 2017a) to generalize the viscosity law. Recent simulations (albeit of gas-pressure dominated disks only) indeed seem to show a power-law stress-pressure relation (Sano et al. 2004; Minoshima et al. 2015; Ross et al. 2016; Shadmehri et al. 2018), with an index varying from zero to one according to the different assumptions.

Here, we address this issue generalising the model reported in M03 with:

$$P_{\text{mag}} = \alpha_0 P_{\text{gas}}^\mu P_{\text{tot}}^{1-\mu} \quad (2)$$

where α_0 is a constant, generally not equal to $\alpha_{\text{SS73}} = P_{\text{mag}}/P_{\text{tot}}$. This behavior is physically motivated by the MRI prescriptions, as its growth rate was shown to depend on the $P_{\text{rad-to-}}P_{\text{gas}}$ ratio (Blaes & Socrates 2001; Turner et al. 2002) influencing the level of the magnetic field saturation. Equations (1) and (2) provide the closure equation of the disk-corona system:

$$f = \sqrt{\frac{2\alpha_0}{k_1^2}} \left(1 + \frac{P_{\text{rad}}}{P_{\text{gas}}} \right)^{-\mu/2} \quad (3)$$

where $k_1 = 3k_0/2b$ gathers the model's uncertainties in an order unity factor (M03). Its exact value only affects f at its maximum ($f_{\text{max}} = \sqrt{2\alpha_0/k_1^2}$) and not the nature of what is described throughout this paper.

The model is then completed with the equation of state:

$$P_{\text{tot}} = P_{\text{gas}} + P_{\text{rad}} = \frac{2\rho k_{\text{B}} T}{m_{\text{p}}} + \frac{aT^4}{3} \quad (4)$$

and with a density- and temperature-dependent opacity $\kappa = \kappa(\rho, T)$. We compute the opacity value self-consistently with the density and temperature at each radius with an iterative process, using as reference stellar opacity tables (at solar metallicity) from the Opacity Project (Seaton et al. 1994; Seaton 1995). This is important since the density and temperature regimes relevant for AGN disks imply opacities that can be significantly different from the electron scattering value (e.g., see Jiang et al. 2016; Czerny et al. 2016; Grzędziński et al. 2017b).

Further, we assume a downward component of the X-ray emission (η) and a disk albedo (a_{disk}), which modify the disk equations from the usual $(1 - f)$ factor (M03; Svensson & Zdziarski 1994) to:

$$1 - \tilde{f} = 1 - f [1 - \eta(1 - a_{\text{disk}})] \quad (5)$$

We here adopt $\eta = 0.55$ and $a_{\text{disk}} = 0.1$, respectively (e.g., Haardt & Maraschi 1993). These are typical values for anisotropic Comptonization in plane-parallel geometry, although more generally the product $\eta(1 - a_{\text{disk}})$ can be a function of the photon index Γ (Beloborodov 1999; Malzac et al. 2001) and of the disk's vertical structure.

For simplicity, we adopt dimensionless units for the black hole mass, the accretion rate, the radial distance and the vertical scale-height:

$$\begin{cases} m = M/M_{\odot} \\ \dot{m} = \frac{\dot{M}}{L_{\text{Edd}}/\epsilon_0 c^2} = m^{-1} \frac{\dot{M} \epsilon_0 c^2}{1.3 \times 10^{38}} \\ r = R/R_{\text{s}} = m^{-1} R c^2 / 2GM_{\odot} \\ h = H/R_{\text{s}} = m^{-1} H c^2 / 2GM_{\odot} \end{cases} \quad (6)$$

The equations for h , mid-plane ρ (g cm^{-3}), P (dyn cm^{-2}) and T (K), with the closure equation for f , are reported in Appendix A in Newtonian approximation (however, see Merloni & Fabian 2003, for a relativistic derivation of the $\mu = 0.5$ case), along with the related radial profiles (Fig. A.1). We note that a constant efficiency of $\epsilon_0 = 0.057$, typical of non-rotating black holes, and a no-torque inner boundary condition ($J(r) = 1 - \sqrt{r_0/r}$, with $r_0 = 3$ and $r_{\text{out}} = 2000$) are initially adopted.

Once m , \dot{m} , α_0 , μ and f_{max} are fixed, one can numerically solve the closure equations for f at each radius (see the last rows of Eqs. (A.1) and (A.3), respectively). The left-hand side is equal to $P_{\text{rad}}/P_{\text{gas}}$ and we can infer the correct regime and compute the main physical quantities at the mid-plane (ρ , P , T , κ). Then, the effective temperature at the surface is computed:

$$T_{\text{eff}}(r) \propto \frac{T(r)}{\tau(r)^{1/4}} \quad (7)$$

where we take $\tau(r) = h(r)\rho(r)\kappa(r)$. Monochromatic optical-UV luminosities can be then easily computed in the multi-color blackbody approximation:

$$L_{\nu}(r) = 2\pi r \Delta r \pi B_{\nu}(T_{\text{eff}}) \quad (8)$$

where $\pi B_{\nu}(T_{\text{eff}})$ is the black-body flux at the frequency ν and temperature $T_{\text{eff}}(r)$.

In this framework, the energy per unit area dissipated in the corona at each radius is $Q_{\text{cor}}(r) = f(r)Q_{+}(r)$, although only a

fraction $(1 - \eta)$ will contribute to what is observed as X-ray emission:

$$L_{X,\text{tot}}(r) = 2\pi r \Delta r (1 - \eta) f(r) Q_{+}(r) \quad (9)$$

Here, we did not include the component reflected by the disk (given by the fraction $f\eta a_{\text{disk}}$), so that we could easily extrapolate at each radius a monochromatic value, for instance $L_{2\text{keV}}$, assuming a simple power-law spectrum within $\nu_1 = 0.1$ and $\nu_f = 100\text{ keV}$:

$$L_{X,\text{tot}} = K \int_{\nu_1}^{\nu_f} \nu^{-(\Gamma-1)} d\nu$$

$$L_{2\text{keV}} = K \nu_{2\text{keV}}^{-(\Gamma-1)} = L_{X,\text{tot}} (2 - \Gamma) \frac{\nu_{2\text{keV}}^{1-\Gamma}}{\nu_1^{2-\Gamma} - \nu_f^{2-\Gamma}} \quad (10)$$

The model relies on the assumption that a plane-parallel geometry holds for bright radiatively-efficient sources, lying in a sweet spot of accretion rate (\dot{m} approximately from a few percent to Eddington). Hence, the accretion disk extends down to the innermost stable circular orbit (ISCO) and no advection is included. A scripted version of the model outlined in this section will be made publicly available online¹.

2.1. Radial profiles for f and $L_{2\text{keV}}$

In Fig. 1 we show as an example radial profiles of f and $L_{2\text{keV}}$, obtained by solving Eqs. (A.1), (A.3), (9) and (10). For simplicity, we fixed $\alpha_0 = 0.02$ and $f_{\text{max}} = 0.5$ and used the three values of μ corresponding to the most-used viscosity laws, namely $\mu = 0, 0.5$ and 1 , for P_{mag} proportional to P_{tot} , $\sqrt{P_{\text{gas}} P_{\text{tot}}}$ and P_{gas} , respectively. Other values of μ would support the same picture with analogous intermediate profiles. A range of typical m , \dot{m} and X-ray spectral slopes was chosen, following the distribution of objects observed in the survey field adopted for the observational test (see Sect. 4 below), namely with median values (and related 16th and 84th percentiles) of $\log m = 8.7^{+0.4}_{-0.5}$, $\dot{m} = 0.2^{+0.5}_{-0.1}$ and $\Gamma = 2.1 \pm 0.1$.

The solid (or solid-dashed) lines represent the median profiles, with the corresponding shaded areas showing the 16th and 84th percentiles of the distribution. The top panel of Fig. 1 shows how the standard $\mu = 0$ law (e.g., SS73) results in $f = f_{\text{max}}$ at all radii (e.g., Svensson & Zdziarski 1994), whereas alternative viscosity laws (e.g., $\mu = 0.5$ and $\mu = 1$) show non-constant radial profiles for f : in the latter cases, the fraction of power dissipated in the corona is smaller in the regions strongly dominated by P_{rad} . As it was shown in M03 in particular for the $\mu = 0.5$ scaling, the higher suppression of the growth rate in P_{rad} -dominated regions of the disk leads to such damped f -profiles. This directly influences the strength of the corona emission, as $L_{2\text{keV}}$ is proportional (through $L_{X,\text{tot}}$) to the product of f and Q_{+} : Q_{+} peaks at small radii in a very similar way across all models, therefore the ones with deeper f -profiles show flatter $L_{2\text{keV}}$ radial profiles and, hence, weaker coronae (bottom panel of Fig. 1). The exact shape of $f(r)$ also affects the strength of the disk emission since the two are self-consistently coupled (see Eq. (5)).

We can also define the mean value of each $f(r)$ profile (i.e. for each combination of m , \dot{m} and Γ):

$$\langle f \rangle_i = \frac{\int f_i(r) Q_{+,i}(r) 2\pi r dr}{\int Q_{+,i}(r) 2\pi r dr} \quad (11)$$

¹ <https://github.com/rarcodia/DiskCoronasim>

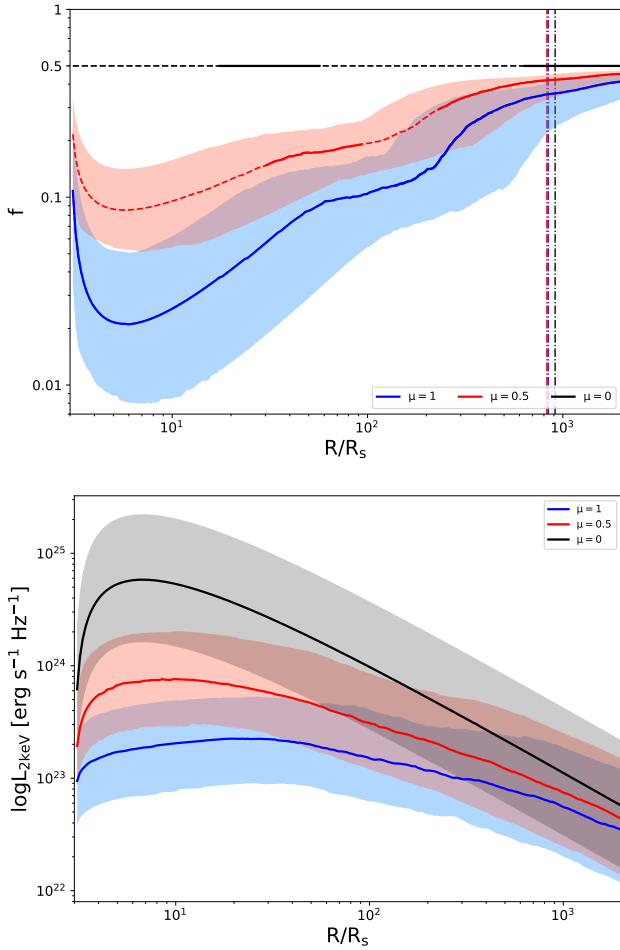


Fig. 1. Radial profiles for the fraction f of power dissipated in the corona (*top panel*) and $L_{2\text{keV}}$ (*bottom panel*), obtained with fixed $\alpha_0 = 0.02$ and $f_{\text{max}} = 0.5$. Colors are coded according to the choice of the viscosity law: stress proportional to P_{tot} ($P_{\text{gas}} + P_{\text{rad}}$, $\mu = 0$, black), to P_{gas} ($\mu = 1$, blue), or the geometric mean of the two ($\mu = 0.5$, red). The continuous solid, or solid-dashed, lines represent the median profiles, with the related shaded areas showing the 16th and 84th percentiles, the scatter due to the range of sources (i.e. m and \dot{m}) modeled. $L_{2\text{keV}}$ is proportional to the product of f and Q_+ (the accretion power per unit area). As Q_+ has very similar profiles across all models, those systems for which f is smaller produce weaker coronae in the central part. *Top panel*: a solid line for the median f -profile represents (thermally) stable regions of the median test source, whereas a dashed line highlights the instability regions. The vertical dot-dashed lines show instead where the median transition radius, from P_{rad} - to P_{gas} -dominated regions, lies. Refer to Sect. 2.1 for details.

that is also a function of μ , α_0 and f_{max} . Then, the mean value can be computed for the median f profiles in the examples in the top panel of Fig. 1: $\langle f \rangle_{\text{median}} = 0.5, 0.13$ or 0.05 , for $\mu = 0, 0.5$ and 1 , respectively. Of course, within such a model the exact value of $\langle f \rangle_{\text{median}}$ depends on its normalization f_{max} , that is a free parameter in the model only bound to be < 1 . Nonetheless, simply from looking at $\langle f \rangle_{\text{median}}$ as a function of μ (and from Fig. 1) we can see how, for the same set of inputs (e.g., m, \dot{m}), the different accretion prescriptions relate to the output corona luminosities: in a nutshell, going from $\mu = 0$ to $\mu = 1$ produces lower $\langle f \rangle_{\text{median}}$, thus weaker coronae.

Changing μ also affects the logarithmic scatter in the radial profiles, from being absent in $\mu = 0$ to increase with μ for $\mu \neq 0$ (see Fig. 1). The spread on a given $f(r)$ is due to the scatter in

m, \dot{m} and Γ , where the major role is played by the accretion rate (e.g., see Fig. 1 in M03). Crucially, $\langle f \rangle$ decreases with increasing \dot{m} for all $\mu \neq 0$ models. This points in the same direction as the evidence of an X-ray bolometric correction (that is proportional to the inverse of f) increasing with the accretion rate (e.g. Wang et al. 2004; Vasudevan & Fabian 2007, 2009; Lusso et al. 2010; Young et al. 2010). This relation between $\langle f \rangle$ and \dot{m} has also crucial implications for what our models predictions on the physical mechanisms behind the observed L_X-L_{UV} (see Sect. 3).

2.2. Local thermal stability

Before proceeding to a detailed observational test of the model, we briefly discuss here the stability issue for the various adopted viscosity laws. Jiang et al. (2016) showed that the presence of the iron bump in the opacity at $\sim 2 \times 10^5$ K stabilizes the flow in the disk regions around that temperature, where the cooling term has a different dependency and thermal runaway is avoided (Grzędzielski et al. 2017b). In the top panel of Fig. 1, a solid median line for the f -profile represents (thermally) stable regions of the median test source, whereas a dashed line highlights the instability regions. The vertical dot-dashed lines show instead where the median transition radius, from P_{rad} - to P_{gas} -dominated regions, lies. This highlights that, for the median test source, the stability region extends also well within P_{rad} -dominated regions of the disk, confirming previous results (Jiang et al. 2016; Grzędzielski et al. 2017b). More quantitatively, we computed the thermal stability balance (e.g. Pringle 1976) for each test source (m, \dot{m}) at all radii with varying viscosity laws. The new stability regions in the inner P_{rad} -dominated portions of $\mu = 0$ and $\mu = 0.5$ disks are ubiquitous, but they appear at different radii according to where the disk reaches the temperatures around the iron bump in κ (see also Fig. A.1). The $\mu = 1$ case, as it is well known (e.g. Lightman & Eardley 1974), is stable throughout.

3. Predictions of the model on the L_X-L_{UV} relation

In this section we aim to test our disk-corona model (presented in Sect. 2) against the observed L_X-L_{UV} , a robust observable linked to the disk-corona physics. Before performing a more quantitative observational test (Sect. 4), we here outline the predictions of our model concerning the disk-corona energetics and the expected impact of our accretion prescription on the L_X-L_{UV} .

The schematic illustration in Fig. 2 summarizes the qualitative take-home messages of this work. The observed L_X-L_{UV} states that going from a lower to a higher accretion regime, the luminosity of the corona increases less than the disk luminosity, resulting in a slope smaller than one in the log-space. In our model for the disk-corona system, the luminosity outputs are directly modified by the viscosity prescription in the flow, determined by the parameter μ , and by the fraction of accretion power going into the corona, f (see Table 1 for a summary on the model parameters). Among all scenarios spanned by these two main unknowns, the qualitative behavior of the accretion disk-corona system, along its radial extent, is similar: higher accretion states have a more powerful disks and coronae, but wider P_{rad} -dominated inner region and, only for modified viscosity prescriptions (i.e. $\mu \neq 0$), lower relative contribution of the corona to the total luminosity (see the upper diagram in Fig. 2).

Thus, our model can provide a simple explanation for the observed slope of the L_X-L_{UV} relation, bridging in a simple but effective way the gap between the observed X-to-UV energetics and some aspects of MRI simulations. Changing μ not only

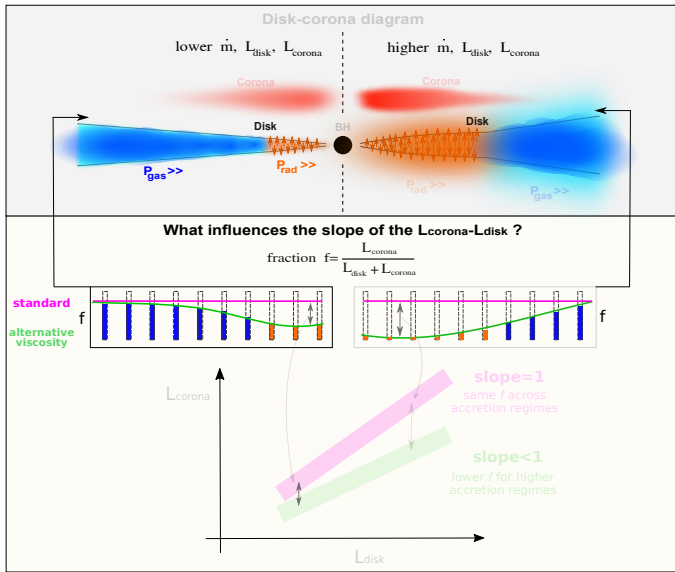


Table 1. Summary of recurring model parameters.

Parameter	Definition	Comments
μ	Regulates the scaling between the magnetic stress and the thermal pressure: $\tau_{r\phi} \propto P_{\text{mag}} = \alpha_0 P_{\text{gas}}^\mu P_{\text{tot}}^{1-\mu}$	$\mu = 0 \rightarrow P_{\text{mag}} \propto P_{\text{tot}}$ $\mu = 0.5 \rightarrow P_{\text{mag}} \propto \sqrt{P_{\text{gas}} P_{\text{tot}}}$ $\mu = 1 \rightarrow P_{\text{mag}} \propto P_{\text{gas}}$
α_0	Proportionality constant of the viscosity law (see above)	Small influence on L_X-L_{UV}
$f(r)$	Fraction of accretion power dissipated in the corona	$f(r)$ for $\mu \neq 0$
f_{max}	Maximum value of $f(r)$	Impacts the normalization of the L_X-L_{UV}
$\langle f \rangle$	Mean value of a $f(r)$ profile	Real fraction of bolometric power emitted by the corona
η	Fraction of f emitted downward back to the disk	Exact value impacts the normalization of the L_X-L_{UV}

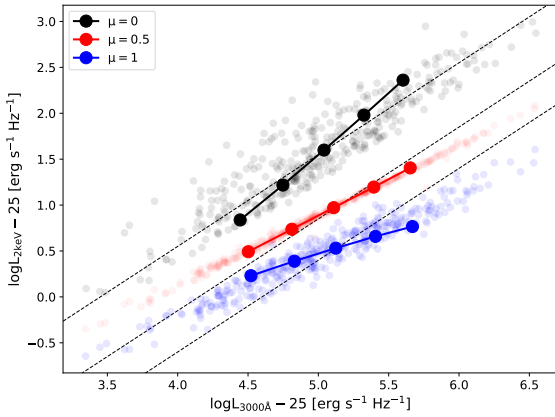


Fig. 3. Mock L_X-L_{UV} with fixed $f_{\text{max}} = 0.5$ and different μ color coded, as in Fig. 1. The connected solid points show the trend of a single typical mass ($\log m = 8.7$) with $\dot{m} = 0.03, 0.07, 0.17, 0.42, 1$ (increasing from left to right in L_{UV}). The dashed lines indicate a slope of one. The distributions of transparent points show the mock L_X-L_{UV} for a range of $\log m = 8.7^{+0.4}_{-0.5}$, $\dot{m} = 0.2^{+0.5}_{-0.1}$ and $\Gamma = 2.1 \pm 0.1$, that follows the typically observed objects (see Sect. 4).

Then, to exclude data contaminated by X-ray absorption, not accounted for in our modeling, we conservatively selected only sources in which the 84th percentile of the N_H posterior distribution was smaller than $10^{21.5} \text{ cm}^{-2}$, a value typically adopted to distinguish X-ray obscured and un-obscured sources (Merloni et al. 2014; see also Della Ceca et al. 2008).

Finally, we take $L_{2\text{keV}}$ as reference for the corona emission in the L_X-L_{UV} . In the model, we computed mock $L_{X,\text{tot}}$ with no reflection, so that we could easily extrapolate $L_{2\text{keV}}$ assuming a simple power-law spectrum. However, in L16 the reflection component was also included in the calculation of $L_{2-10\text{keV}}$, as it is usually observed both in low- z (e.g. Nandra et al. 2007) and high- z (e.g. Baronchelli et al. 2018) spectra (see the average-AGN model in Buchner et al. 2014). Therefore, we consistently excluded from the analysis all the sources with a significant reflection component: given the high errors of the typical $\log R$ fit in L16³, we included only sources in which the 16th percentile was < -0.2 and the 84th was < 0.5 . We note that L16 included in the fit also a scattering contribution from ionized material inside the angle of the torus (see Buchner et al. 2014), although the fit normalizations are on the order of 10^{-4} with respect to the main power-law component.

The final cleaned subsample, to which we will refer as XMM-XXL, consists of 379 sources with observed m (with

³ R is the ratio of the normalization of the reflection component with respect to the power-law component.

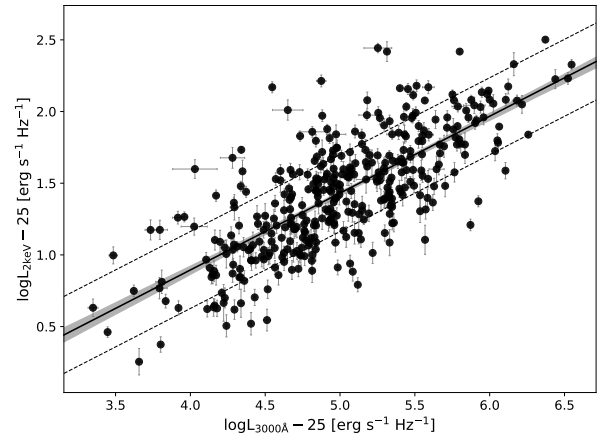


Fig. 4. L_X-L_{UV} relation of the 379 bright BLAGN of XMM-XXL. Monochromatic luminosity values are here scaled by 25 dex, to ease the comparison with recent works. The solid black line is the median regression line obtained with emcee, with the corresponding 16th and 84th percentiles represented with the shaded gray area. The dashed black lines show the intrinsic scatter around the median relation.

median $\log m = 8.7^{+0.4}_{-0.5}$, $L_{3000\text{\AA}}$, Γ (with median $\Gamma = 2.1 \pm 0.1$) and $L_{2\text{keV}}$. In Fig. 4 we show the $\log L_X = \hat{\alpha} + \hat{\beta} \log L_{UV}$ relation, with the best-fit linear regression given by:

$$\log L_{2\text{keV}} - 25 = (-1.25 \pm 0.12) + (0.54 \pm 0.02) (\log L_{3000\text{\AA}} - 25) \quad (12)$$

with intrinsic scatter $\sigma_{\text{intr}} = 0.27 \pm 0.01$. Linear regressions in two (or more) dimensions were performed with emcee (Foreman-Mackey et al. 2013), accounting for uncertainties on all variables and an intrinsic scatter using the likelihood provided in D’Agostini (2005). The uncertainty in the independent variable(s) is propagated with the derivative $\partial Y/\partial X$ calculated in $X(X_i)$, equal to the slope coefficient(s) in the linear case (D’Agostini 2003). The slope we measure is slightly flatter than what is quoted in the recent literature (e.g., Lusso & Risaliti 2016), although we did not consider all the possible biases of flux-limited samples (however, see Appendix B). For the main scope of this paper, it is sufficient to have a reference sample cleaned in accord with the physics described within the model.

4.2. Methodology of the observational test

In our model $\dot{m} = \lambda_{\text{edd}} = L_{\text{bol}}/L_{\text{edd}}$, although we do not take as reference also \dot{M} or λ_{edd} from L16: the former is interpolated from the mass and a monochromatic optical luminosity (Davis & Laor 2011), while the latter depends on a

disk-luminosity estimate via L_{bol} . Both approaches are based on standard-disk assumptions or calculations and using those values within our non-standard disk models would be an inconsistency. One can also estimate L_{bol} applying bolometric corrections (BC) to the observed monochromatic optical-UV luminosities (Richards et al. 2006; Runnoe et al. 2012), although the many uncertainties in play (Krawczyk et al. 2013; Kilerci Eser & Vestergaard 2018) and the high scatter in the BCs (Richards et al. 2006; Lusso et al. 2012) discouraged us in relying on this approach. Then, for every source we iteratively obtain the \dot{m} value yielding a model $L_{3000\text{\AA}}$ consistent with the observed one within its errors (typically ~ 0.01 dex). This approach is similar to the interpolation method put forward by Davis & Laor (2011), although we do it consistently for each different model, which is given by a choice of μ , α_0 and f_{max} .

The methodology then consists in fixing μ , α_0 and f_{max} (see Table 1 for a summary on the model's parameters), which will be referred to as the model choice, within a discrete 3D grid in $\mu = [0, 0.2, 0.4, 0.5, 0.6, 0.8, 1]$, $\alpha_0 = [0.02, 0.2]$ and $f_{\text{max}} = [0.1, 0.2, 0.3, 0.5, 0.7, 0.9, 0.99]$. Then, we take as input m , Γ and $L_{3000\text{\AA}}$ from the observed data, allowing us to solve the equations of the model for each source and compute \dot{m} and $L_{2\text{keV}}$ values (see Sect. 2). For each observed source of the reference sample, every model in the 3D grid can provide a mock entry for the L_X-L_{UV} . A proper comparison requires uncertainties to be assigned on the mocks, as the observed m , Γ and $L_{3000\text{\AA}}$ come with their own measurement and systematic errors, where obviously the $\sim 0.4-0.5$ dex systematics in the mass estimates (e.g. Shen 2013, and references therein) play the dominant role. As it is mentioned above, mock $L_{3000\text{\AA}}$ values converge to the related observed quantities within their errors, hence we conservatively fixed the mock $\delta L_{3000\text{\AA}}$ at the 90th percentile of the uncertainty distribution in the observed $L_{3000\text{\AA}}$ (i.e. ~ 0.03 dex). In order to compute uncertainties for \dot{m} and $L_{2\text{keV}}$, we ran each model 200 times on the same source, extracting the input values (m , Γ and $L_{3000\text{\AA}}$) from a normal distribution with mean and standard deviation taken from the observed quantities and their errors. Then, the uncertainty on \dot{m} and $L_{2\text{keV}}$ is taken from the dispersion of the 200 runs.

5. Results of the observational test

For all the models on the discrete 3D grid in the μ , α_0 and f_{max} parameter space (see Sect. 4.2 and Table 1), we fit the L_X-L_{UV} distribution with a log-linear relation $\log L_X = \hat{\alpha} + \hat{\beta} \log L_{\text{UV}}$. Three examples are shown in Fig. 5 for μ corresponding to the known analytic viscosity prescriptions (see Sect. 2). Ideally, a model should reproduce the observed L_X-L_{UV} in both normalization and slope. However, we can start decomposing the problem in two parts: a good match in the normalization ($\hat{\alpha}$) would state that globally, for a given optical-UV luminosity distribution, the modeled corona emission was strong enough (see Sect. 5.1); instead, if the slope ($\hat{\beta}$) is matched, then the model accurately describes how the coronal strength varies from lowly- to highly-accreting sources (see Sect. 5.2). Moreover, as it can be seen from the examples in Fig. 5, our models come with their one intrinsic scatter, given by different m and Γ at a fixed \dot{m} . This provides precious insights on the nature of the total observed scatter (see Sect. 5.3).

5.1. The normalization of the L_X-L_{UV}

First, we investigate how well the mocks reproduce the data normalization along the vertical axis of the L_X-L_{UV} . To do so, we

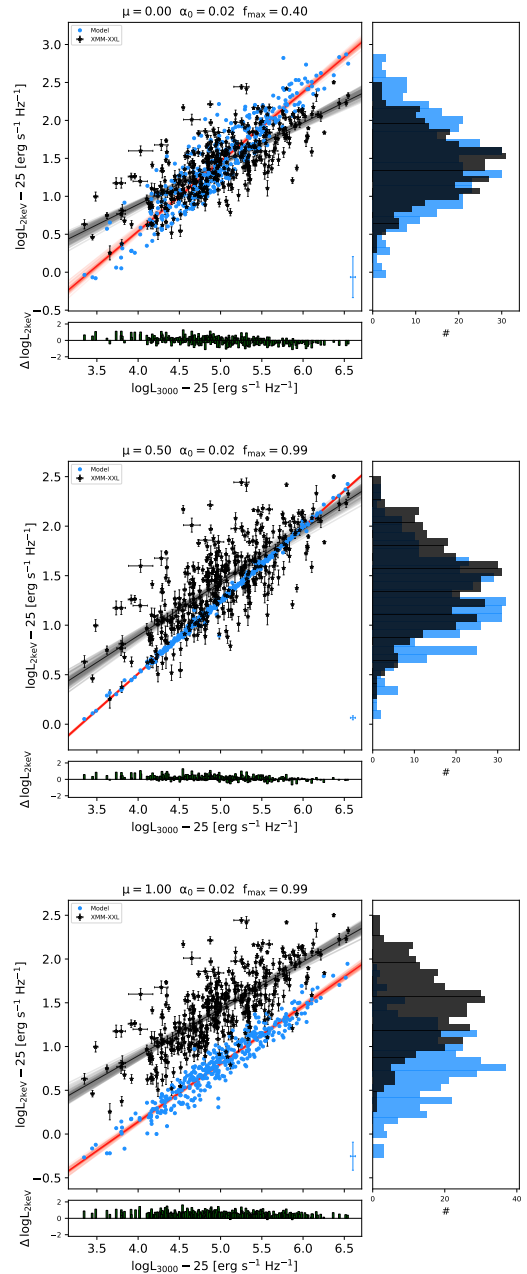


Fig. 5. The central panel of each image shows an example of the L_X-L_{UV} relation for both XMM-XXL (black stars) and the model (blue dots), in which the choice of μ , α_0 and f_{max} is shown in the titles. The black and red solid lines are randomly drawn from the posterior distributions of normalization and slope for XMM-XXL and the model, respectively, with the median regression line thickened. The bottom panels show the residuals given by the difference of observed and mock $\log L_{2\text{keV}}$ and the right panels show the related distributions. The errors on the model are shown in the bottom right corner of the central panels.

define a score for the goodness of match:

$$r_i^2 = 1 - \frac{\sum_i (y_{\text{data},i} - y_{\text{mock}_i})^2}{\sum_i (y_{\text{data},i} - \langle y_{\text{data}} \rangle)^2} \quad (13)$$

The r^2 score is computed drawing 1000 random samples from the observed $\log L_{2\text{keV}}$ within their errors (i.e. $y_{\text{data},i}$), and 1000 random regression lines from emcee's chains on the mock

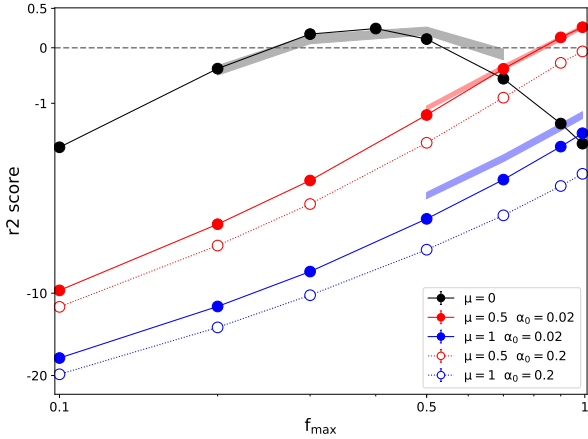


Fig. 6. r^2 score, representing the goodness of match between XMM-XXL and mocks (see text), as a function of f_{\max} . Models with $\mu = 0, 0.5, 1$ are color coded in black, red and blue, respectively. The additional dependency on α_0 is represented with varying line-types as shown in the legend, when present (it is absent for $\mu = 0$). A good match is represented with a score greater than zero. The points include the uncertainties in the score values. The shaded areas represent the results obtained applying the same methodology on a different sample (RM-QSO, Liu et al., in prep.), fixing $\alpha_0 = 0.02$ and using the same colors.

(i.e. y_{mock_i}). Then, the median and the 84th–16th inter-quantile range are quoted from the resulting distribution of 1000 r_i^2 scores. Negative scores indicate the data are poorly reproduced by the model; an $r^2 = 0$ would be obtained by a constant value corresponding to the mean of the observed $\log L_{2\text{keV}}$ distribution. We can put a quality threshold and keep all the models that yield a positive score.

The r^2 score as a function of f_{\max} is shown in Fig. 6, where the choice of μ is color coded and the additional dependency on α_0 is represented with varying line-types (it is minor or absent, as in $\mu = 0$). We show for simplicity only values of μ corresponding to the known analytic viscosity prescriptions (see Sect. 2). The other values used would accordingly show intermediate results. For each viscosity law there is a preferred f_{\max} , that fixes the maximum coronal strength in a model.

Models with higher μ need higher normalization f_{\max} , since they have a comparably weaker X-ray emission, in accord with their lower $\langle f \rangle_{\text{median}}$ (see Fig. 1 and Sect. 2.1). Nonetheless, the law correspondent to $\mu = 1$ does not produce adequately strong coronae even with $f_{\max} = 0.99$ and can be ruled out (see right image in Fig. 5). Furthermore, $\mu = 1$ produces a radially flatter X-ray emission profile (see bottom panel of Fig. 1), in contrast with observations that hint for coronae peaking in the inner radii (e.g. Mosquera et al. 2013; Reis & Miller 2013; Wilkins et al. 2016). We explore this behavior more quantitatively in the top panel of Fig. 7 showing how the radius of the annulus at which the 2 keV emission peaks (r_{peak} , or at which it is 90% of the total, r_{90}) varies with μ : as μ increases, most of the corona emission comes from annuli placed at larger and larger radii.

We also verified that our results do not depend on the sample adopted as reference. We performed the same analysis with the RM-QSO sources (Liu et al., in prep.; Shen et al. 2019), on which a similar analysis was performed and on which we applied compatible cleaning criteria and methodology, as described in Sects. 4.1 and 4.2. The results are shown in the r^2 score plot (Fig. 6) with shaded areas, color coded for μ in the same way and using only $\alpha_0 = 0.02$. There is generally a good agreement between the two samples, suggesting that our results are not dependent from the different data used.

It is worth stressing that the f_{\max} value at which each μ (possibly) matches the observed normalization is degenerate with the assumptions on the accretion efficiency and on the product $\eta(1 - a_{\text{disk}})$. Namely, higher accretion efficiencies and/or a higher fraction of the coronal emission beamed away from the disk would increase the normalization of the L_X – L_{UV} relation, and shift all curves of Fig. 6 to the left. This will be further examined in Sects. 5.6 and 5.7.

5.2. The slope of the L_X – L_{UV}

Figure 6 allows us to track the models (i.e. combinations μ , α_0 and f_{\max} , see Table 1) that broadly reproduce the normalization $\widehat{\alpha}$ of the observed L_X – L_{UV} . Nonetheless, obtaining the correct normalization is simply a weighting exercise of the energetic outputs of the disk and the corona. It is the slope that carries the exact information on how the disk-corona interplay changes across the different accretion regimes of bright radiatively-efficient AGN (see Sect. 3). This would require a precise knowledge of the true slope of the L_X – L_{UV} . The observations suggest a value around ≈ 0.6 (Lusso & Risaliti 2016; LR17; our Appendix B) and we can acknowledge this value as reference. Our methodology, however, can be regarded as data-independent, and it would be applicable even if future works will update the current knowledge on the exact value of the slope.

In the middle panel of Fig. 7 we show how the modeled slope of the L_X – L_{UV} gets closer to the observed one for increasing μ (i.e. for more damped radial f -profiles), for a fixed $\alpha_0 = 0.02$ and using only the f_{\max} corresponding to the highest r^2 -score. This is because models with increasing μ have higher logarithmic scatter in $f(r)$, meaning that going from lowly- to highly-accreting sources the span in $\langle f \rangle_i$ is larger, with high- \dot{m} objects having comparably weaker X-ray emission with respect to low- \dot{m} companions (see Sect. 3). We show this for $\mu = 0, 0.5$ and 1, respectively⁴:

$$\begin{aligned} \log \langle f \rangle &= \log f_{\max} \\ \log \langle f \rangle &= (-1.12 \pm 0.24) - (0.15 \pm 0.02) \log \dot{m} \\ &\quad + (0.05 \pm 0.03) \log m \\ \log \langle f \rangle &= (-1.82 \pm 0.36) - (0.27 \pm 0.03) \log \dot{m} \\ &\quad + (0.07 \pm 0.04) \log m \end{aligned} \quad (14)$$

where the steepest dependency from \dot{m} is obtained for larger μ .

This test points in the same direction as the evidence of an X-ray bolometric correction increasing with the accretion rate (e.g. Wang et al. 2004; Vasudevan & Fabian 2007, 2009; Lusso et al. 2010; Young et al. 2010), although we refrain to compare this observable with our regressions (e.g. Wang et al. 2004; Cao 2009; Liu & Liu 2009; You et al. 2012; Liu et al. 2012, 2016a), due to the many more uncertainties in play when deriving bolometric luminosities in comparison to the quantities entering in the L_X – L_{UV} (see the discussion in Sect. 4.2).

5.3. The scatter of the L_X – L_{UV}

The observed scatter of the L_X – L_{UV} for the sample used in this work is $\sigma_{\text{intr}} = 0.27 \pm 0.01$ (Sect. 4.1). As a matter of

⁴ The distributions of mock \dot{m} are very similar across the models, with median values (and related 16th and 84th percentiles) of $0.16_{0.04}^{0.69}$, $0.15_{0.05}^{0.65}$ and $0.14_{0.04}^{0.59}$ for $\mu = 0, 0.5$ and 1, respectively. The tails include Eddington or even super-Eddington sources. We note that the uncertainty on the modeled \dot{m} , propagated through the ones in the observations, is as large as ≈ 0.65 dex.

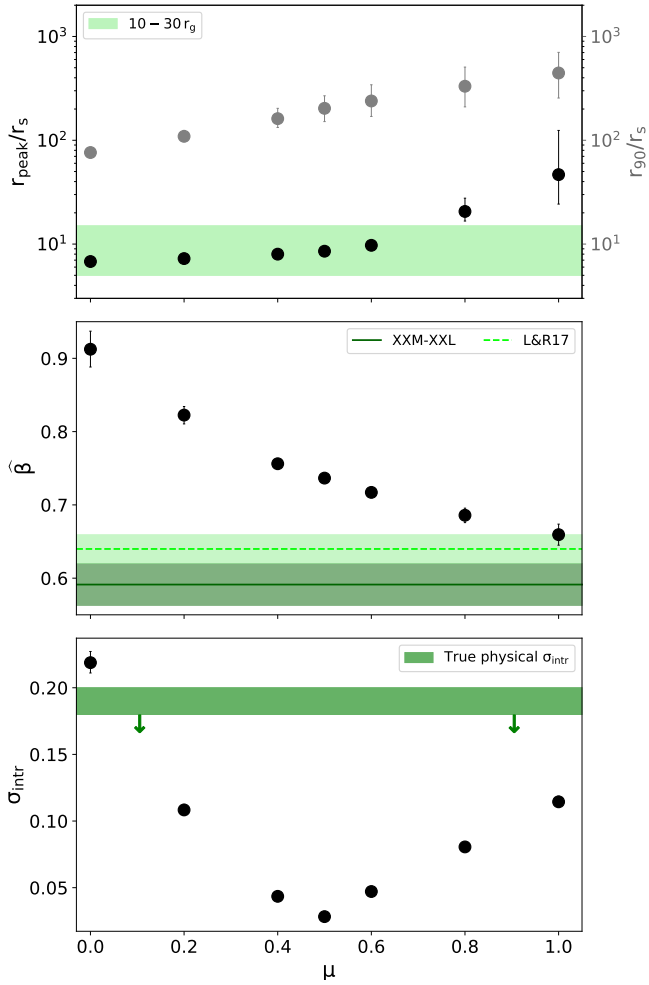


Fig. 7. *Top panel:* the 2 keV-emission r_{peak} (r_{90}) as a function of μ is represented in black (gray). The green shaded area qualitatively shows the inner radii, where the bulk of X-ray emission is supposed to come from according to X-ray reverberation and micro-lensing. For increasing μ , the X-ray emission profile peaks at larger radii. *Middle panel:* for increasing μ the models obtain a slope of the L_X - L_{UV} closer to the observed one. The dark-green area represents the reference slope of the cleanest XMM-XXL (Appendix B), while the light-green refers to the slope quoted in LR17. *Bottom panel:* intrinsic scatter of the mock L_X - L_{UV} relations as a function of μ . The green area represents a tentative upper limit of the true scatter (Lusso & Risaliti 2016; Chiaraluce et al. 2018), that is only due to the physical properties of AGN. For simplicity, all panels show only the results obtained with a single f_{max} , corresponding to the highest r^2 -score (e.g., Fig. 6), and fixed $\alpha_0 = 0.02$.

fact, this value represents an upper limit to the intrinsic dispersion inherent to the physics of the system, as the observed scatter is affected by a combination of instrumental and calibration issues, UV and X-ray variability, non-simultaneity of the multi-wavelength observations. A lot of effort has been put into trying to quantify as accurately as possible all these contaminants (e.g. Vagnetti et al. 2013; Lusso 2019, and references therein), with claims that the intrinsic scatter in the L_X - L_{UV} relation is smaller than $\lesssim 0.18$ - 0.20 (Lusso & Risaliti 2016; Chiaraluce et al. 2018). Any successful model should be able to reproduce such a low scatter.

From the examples of mock L_X - L_{UV} relations plotted in Fig. 5, it can already be seen that our models come with their one intrinsic scatter. In our methodology (Sect. 4.2), the modeled

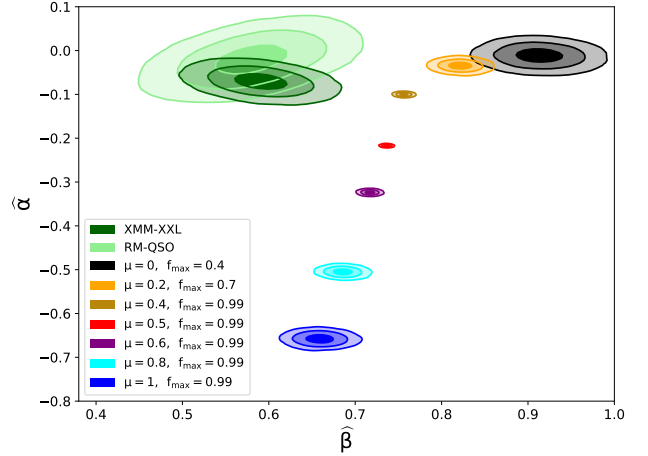


Fig. 8. 1-, 2- and 3-sigma contours of the emcee regressions in the slope-normalization ($\hat{\beta} - \hat{\alpha}$) plane of the L_X - L_{UV} for both data and models, normalizing all L_X and L_{UV} to the corresponding median values of XMM-XXL. Dark green contours are related to the cleanest XMM-XXL sample (Appendix B) and the light green ones to the RM-QSO sources. The contour of the models are color coded for $\mu = [0, 0.2, 0.4, 0.5, 0.6, 0.8, 1]$, as shown in the legend. For simplicity, we report for each μ only results obtained with a single f_{max} , corresponding to the highest r^2 -score, and fixed $\alpha_0 = 0.02$. Models that reproduce the observed slope $\hat{\alpha}$ are also the ones that show weaker coronae (lower normalization $\hat{\alpha}$).

\dot{m} was tuned to the observed $L_{3000\text{\AA}}$, hence the intrinsic scatter of the mock L_X - L_{UV} relations is simply the dispersion of the modeled $L_{2\text{keV}}$, at a given \dot{m} , due to different \dot{m} and Γ . We show this more quantitatively in the bottom panel of Fig. 7. The models dispersion varies with μ because changing the viscosity law induces a different logarithmic scatter in $f(r)$ (see Fig. 1) and it also affects the distance (in gravitational radii) from which the bulk of the $L_{2\text{keV}}$ is coming (see top panel of Fig. 7). The resulting σ_{intr} of the models is likely a complex combination of these (and possible more) factors. All the models, with the exception of $\mu = 0$, lie below the available observational constraints (Lusso & Risaliti 2016; Chiaraluce et al. 2018) of $\lesssim 0.18$ - 0.20 . This is another successful prediction of our model (see Sect. 3).

5.4. A complete picture: the slope-normalization plane of the L_X - L_{UV}

In the previous sections, we decomposed the match in either normalization or slope to have a better understanding on how our disk-corona models can relate to the observed L_X - L_{UV} . However, the goal would be to have a model that can fully encompass these observables. Hence, in Fig. 8 we display 1-, 2- and 3-sigma contours in the slope-normalization plane ($\hat{\beta} - \hat{\alpha}$) of the L_X - L_{UV} for both data and models. All regressions were performed with emcee normalizing both L_X and L_{UV} to the median value of XMM-XXL. The data contours are related to the cleanest XMM-XXL version (Appendix B) and to the RM-QSO sources⁵. Model contours are shown for $\mu = [0, 0.2, 0.4, 0.5, 0.6, 0.8, 1]$ using a single f_{max} , corresponding to the highest r^2 -score (e.g., Fig. 6) for each μ , and a fixed $\alpha_0 = 0.02$, for simplicity.

⁵ XMM-XXL luminosities were obtained in L16 including a Balmer continuum component in the fit (refer to Shen & Liu 2012), although for the RM-QSO this component was switched off (Shen et al. 2019). For consistency, a rigid shift of -0.12 dex was applied to the RM-QSO $L_{3000\text{\AA}}$ (Shen & Liu 2012) for obtaining the contours displayed in Fig. 8.

Figure 8 shows that models reproducing the observed slope, namely the ones with higher μ (as in middle panel of Fig. 7), are also the ones that show weaker coronae (lower normalization $\bar{\alpha}$) and overly extended $L_{2\text{keV}}$ -emission (i.e. higher r_{peak} and r_{90} , top panel of Fig. 7).

5.5. The 3D plane: L_X vs L_{UV} vs m

As shown by LR17, the L_X - L_{UV} relation for AGN is rather a three-dimensional problem, with the mass (or its proxy given by the full-width half-maximum of broad emission lines) playing a significant role as well. The observed L_X - L_{UV} - m plane from XMM-XXL can be fit by:

$$\log L_{2\text{keV}} - 25 = (-0.91 \pm 0.13) + (0.39 \pm 0.03) (\log L_{3000\text{\AA}} - 25) + (0.23 \pm 0.04) (\log m - 7) \quad (15)$$

and the mock L_X - L_{UV} - m from models with $\mu = 0, 0.5$ and 1 , respectively:

$$\log L_{2\text{keV}} - 25 = (-3.49 \pm 0.15) + (1.08 \pm 0.03) (\log L_{3000\text{\AA}} - 25) - (0.27 \pm 0.03) (\log m - 7)$$

$$\log L_{2\text{keV}} - 25 = (-2.41 \pm 0.15) + (0.73 \pm 0.01) (\log L_{3000\text{\AA}} - 25) + (0.013 \pm 0.004) (\log m - 7)$$

$$\log L_{2\text{keV}} - 25 = (-2.28 \pm 0.08) + (0.57 \pm 0.02) (\log L_{3000\text{\AA}} - 25) + (0.14 \pm 0.02) (\log m - 7) \quad (16)$$

The comparison in the 3D plane states that the exact dependency is not obtained by any of the models, with $\mu = 1$ being the closest in qualitatively retrieving the coefficients for $L_{3000\text{\AA}}$ and m . We note that the mass is taken from the observations, thus this mismatch states that the luminosities in the model do not depend on the mass in the correct way.

5.6. The impact of the accretion efficiency

Throughout this work we adopted an efficiency $\epsilon_0 = 0.057$, typical of non-rotating black holes (e.g. Shapiro 2005), for simplicity. Nonetheless, a high spin seems to be preferred to model the blurred relativistic iron line, detected both in the local Universe (Nandra et al. 2007; Reynolds 2013) and up to $z \sim 4$ (e.g. Baronchelli et al. 2018). Moreover, flux-limited samples are known to be biased in preferentially detecting high-spinning black holes (Brenneman et al. 2011; Vasudevan et al. 2016), simply because they are brighter than their non-rotating analogous (see Reynolds 2019).

Then, we tested the model using maximally-spinning black holes, with radiative efficiency 0.3 and ISCO down to $r_0 = 1.24r_g$ (Thorne 1974). This has a major impact on the normalization axis of the L_X - L_{UV} . Everything else in the source being equal, in a spinning black hole matter can be accreted down to smaller distances with respect to their non-rotating companions, thus the accretion power in the system is much higher. As a matter of fact, changing the radiative efficiency has an impact on the numerical equation that regulates $f(r)$: for the same m and \dot{m} and $r > 3$ the values of f is higher, and the transition radius between P_{rad} - and P_{gas} -dominated regions moves at lower radii. This self-consistently affects the disk equations via the $(1 - \tilde{f})$ factor (see Appendix A), hence the surface temperature is decreased at higher radii, where most of the disk emission at 3000\AA comes from. Then, the modeled \dot{m} value needed to match the observed $L_{3000\text{\AA}}$ is higher (see Sect. 4.2) and, consequently, $L_{2\text{keV}} \propto fQ_+$ is higher.

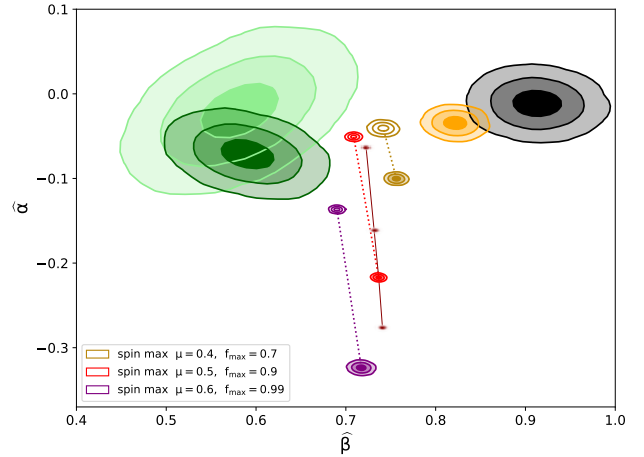


Fig. 9. Same as Fig. 8, with the addition of empty contours for $\mu = 0.4, 0.5$ and 0.6 (color coded in the legend) obtained with maximally spinning black holes (i.e. with $\epsilon_0 = 0.3$ and $r_0 = 1.24r_g$). The dashed lines connect them to the non-spinning analogous realizations. Dark-red density spots represent the location of the center of different contours of the standard $\mu = 0.5$ case, in which the only difference is the adoption of η (downward scattering component) varying among 0.4, 0.5 and 0.6, going from higher to lower $\bar{\alpha}$, respectively.

In Fig. 9 we show the model contours in the correlation slope-normalization plane computed for both low and high radiative efficiency, for $\mu = 0.4, 0.5$ and 0.6 only.

Interestingly, maximally-spinning sources yield a better match with the data contours, in particular for the viscosity law $\mu = 0.5$, with $f_{\text{max}} = 0.9$. For instance, Fig. 10 shows how the data and this high-spin model compare in the L_X - L_{UV} plane. We want to stress that using only a maximum spin for all sources is an extreme measure, but since the (unknown) observed spin distribution is likely dominated by high-spin values (Reynolds 2019), model contours of a more realistic diverse population of high-spinning sources would be closer to the high-efficiency ones in Fig. 9 rather than to the spin-zero case. We also note that, even if the modeled coronae would be somewhat weaker using a realistic spin distribution, with respect to the maximum-spin case, the model with $\mu = 0.5$ can still be realized with a higher $f_{\text{max}} = 0.99$. Thus, we speculate that the new empty red contours in Fig. 9 consist in a fair approximation of a realistic high-spin population model. The tension with the observed L_X - L_{UV} would be significantly relaxed.

5.7. The impact of the downward scattering component

The results shown in Fig. 6 are also degenerate with the assumptions on the value of the product $\eta(1 - a_{\text{disk}})$, that is on the assumed downward component of the X-ray emission (η) and on the disk albedo. The adopted value of $\eta = 0.55$ is typical for anisotropic Comptonization in a plane-parallel corona (Haardt & Maraschi 1993), although it is unclear how much it would change in different geometries or prescriptions. In a patchy corona (Haardt et al. 1994) η would unlikely part significantly from the one in the slab case. The only major difference would rather involve the transmission or absorption by the corona of the radiation reflected by the disk. However, we conservatively excluded from the reference sample adopted in the observational test all the sources with a non-negligible reflection component detected (see Sect. 4.1), allowing us to avoid its complicated modeling. In an outflowing corona (e.g. Beloborodov 1999; Malzac et al. 2001), the ratio between the downward and

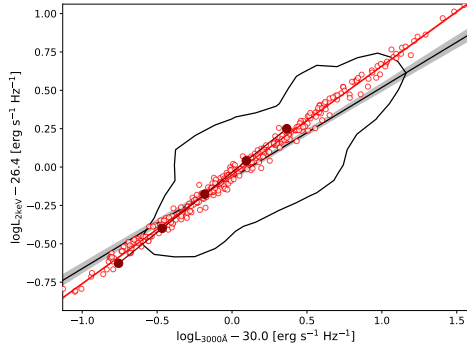


Fig. 10. L_X-L_{UV} relation for the high-spin model with $\mu = 0.5$, $\alpha_0 = 0.02$ and $f_{\max} = 0.9$ (empty red points, corresponding to the empty red contour in Fig. 9), with the red line showing best fit slope from emcee. The connected filled points (dark red) show the single-mass trend ($\log m = 8.7$) for varying accretion rate (0.03, 0.07, 0.17, 0.42, 1). For a comparison, the black contour shows where the data lie in the plane, with the related best-fit slope (black line).

the upward flux decreases with the bulk velocity of the corona (e.g. Janiuk et al. 2000). We tried to quantify possible offsets in the $\widehat{\beta}-\widehat{\alpha}$ plane due to different values of η , ranging from 0.6 (slightly enhanced downward scattering) to 0.4 (reduced downward scattering, roughly approximating an outflowing corona with $\beta_{\text{bulk}} \approx 0.1 - 0.2$, e.g. Janiuk et al. 2000). We show this in Fig. 9 for the $\mu = 0.5$ case, with dark-red density spots ($\eta = 0.4, 0.5$ and 0.6 from higher to lower $\widehat{\alpha}$, respectively). Changing the downward component by $\Delta\eta \sim 0.1$ induces a significant offset of ≈ 0.1 dex in $\widehat{\alpha}$ and a minor change in $\widehat{\beta}$.

6. Discussion

The L_X-L_{UV} relation has been studied for decades (starting with the better-known α_{OX} parameter, Tananbaum et al. 1979), its robustness used for bolometric estimates (e.g. Marconi et al. 2004; Hopkins et al. 2007; Lusso et al. 2010) and recently even for cosmology (Risaliti & Lusso 2015, 2019). Nonetheless, there is currently no solid and exhaustive physical explanation for it. In Sect. 3 we outlined the qualitative predictions of our model and in Sect. 5 we obtained that concordance with current data can be obtained with a modified viscosity prescription in the accretion flow ($\mu = 0.5$), provided the spin of the sources is high. Here, we briefly discuss whether other competing analytic disk-corona models succeed or not and then we try to investigate the impact of the assumptions in our model on the results.

6.1. Comparison with other models

LR17 tried to explain this relation with a very simplified, but effective, toy-model. Most of their assumptions are in common with our work (see Sect. 6.2), although our treatment is more complete and physically motivated. The assumption of the MRI amplifying the magnetic field to a lesser extent in P_{rad} -dominated regions (Blaes & Socrates 2001; Turner et al. 2002; M03) is taken to the extreme with a step function for the f -profile: all the accretion power is emitted by the disk in P_{rad} -dominated regions (i.e. $f(r_{\text{rad}}) = 0$), whereas it is equally distributed between disk and corona in P_{gas} -dominated regions (i.e. $f(r_{\text{gas}}) = 0.5$). The resulting predicted slope and normalization of the L_X-L_{UV} are claimed to be consistent with the observations. The former can be confirmed by our analysis, as their $f(r)$ step-function is nothing but an extremely damped $f(r)$ beyond $\mu = 1$, whose mock slope of the L_X-L_{UV} was the closest

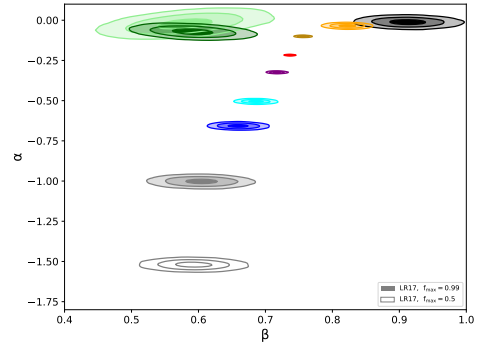


Fig. 11. Same as Fig. 8 with the addition of a reproduction of LR17's toy-model as gray contours.

to the observed one. In the latter case, their match in normalization might be an involuntary artifact: with respect to the power transferred to the corona f , the observed luminosity is roughly halved if a downward scattering component is included (i.e. $f(1 - \eta)$, with $\eta \approx 0.5$). We verified this running our model with $\mu = 0$ and $\alpha_0 = 0.02$, forcing $f = 0$ in the P_{rad} -dominated region and fixing both $f = 0.50$ and $f = 0.99$ in P_{gas} -dominated radii. In Fig. 11 we show the related contours in the $\widehat{\beta}-\widehat{\alpha}$ plane along with our results of Fig. 8. This confirms that their step f -profile results in a slope consistent with the observed value, albeit producing overly weak coronae (too low normalization in the $\widehat{\beta}-\widehat{\alpha}$). Hence, their toy-model does not reproduce the L_X-L_{UV} . Moreover, the X-ray emission from their toy-model inevitably peaks at the transition radius between P_{rad} - and P_{gas} -dominated regions. Indeed, their model with $f_{\text{gas}} = 0.99$ yields $r_{\text{peak}} = 142_{51}^{438}$ and $r_{90} = 790_{445}^{1490}$ (i.e. produces extremely extended coronae).

Kubota & Done (2018) coupled an outer standard disk with an inner warm Comptonising region, that produces the soft X-ray excess, and an innermost hot corona for the hard X-ray continuum. Their model fits remarkably well the broadband continua of three sources spanning a wide range of accretion rates. They also claim to reproduce the observed L_X-L_{UV} , using both the regression line and data points from LR17, although only displaying all the possible sources modeled within a grid of $m = 10^6 - 10^{10}$ and $\dot{m} = 0.03 - 1$ (their Figs. 7 and 8). Nonetheless, first-order normalization matches, even with m and \dot{m} spanning within typical values, can be misleading. A more conclusive test would be, as we do, to match mock and data sources one by one.

6.2. Further assumptions and theoretical uncertainties

Only models with $\mu \lesssim 0.4$ are able to reproduce the observed normalization within the range of possible f_{\max} values, whereas for $\mu \gtrsim 0.5$ they are off by $\gtrsim 0.1 - 0.2$ dex along the normalization. In Sects. 5.6 and 5.7 we showed how a higher accretion efficiency and/or a different downward scattering component may affect our results in the slope-normalization plane. Their impact would be significant and can possibly ease the tension between data and models: high-spin black holes and/or moderately outflowing coronae would be consistent with the observations. We now try to investigate some other simplifications of our model, likely to have a minor or less quantifiable effect on our conclusions.

6.2.1. Soft X-ray excess and thermal instability

The XMM-XXL $L_{2\text{keV}}$ value was interpolated from the $L_{2-10\text{keV}}$ fit in L16 after excluding sources with high reflection fraction (Sect. 4.1). The impact of the soft X-ray excess component

can be considered negligible in that energy range, thus data points in the L_X-L_{UV} are likely not contaminated. However, our models do not include a soft X-ray excess generation mechanism, the monochromatic $L_{2\text{keV}}$ being extracted from a power-law spectrum within 0.1–100 keV. If a significant fraction of the power dissipated in the corona is actually used by a different mechanism producing the observed soft-excess, namely from a warm corona (e.g. Petrucci et al. 2018; Kubota & Done 2018; Middei et al. 2019), the mock $L_{2\text{keV}}$ would be overestimated to an unclear extent. Nonetheless, if the soft X-ray excess is produced by blurred relativistic reflection (e.g. Crummy et al. 2006; Garcia et al. 2019), the influence of this component on our analysis would have been excluded with our selection criteria (Sect. 4.1).

In Sect. 2, we briefly addressed the disk-instability problem (see Fig. 1, top panel) and despite the local stabilizing effect of the iron bump in the opacities, disks with $\mu = 0$ (e.g., SS73) and 0.5 (e.g., M03) are globally unstable in P_{rad} -dominated regions. An intriguing question may be whether the unstable regions in the disk are responsible for generating the soft-excess, possibly within inhomogeneous flows (e.g. Merloni et al. 2006). As a matter of fact, the higher \dot{m} the wider the region where P_{rad} dominates and the higher the soft-excess strength (e.g. Boissay et al. 2016). Nonetheless, a more thorough investigation of this scenario is beyond the reach of this paper.

6.2.2. Magnetically-dominated disks

In our model the stress tensor is dominated by Maxwell stresses as confirmed by simulations (e.g., Hawley et al. 1995; Sano et al. 2004; Minoshima et al. 2015), although the magnetic pressure is bound to be only a fraction of the product $P_{\text{gas}}^\mu P_{\text{tot}}^{1-\mu}$ via α_0 at the mid-plane. However, there are theories postulating disks that are P_{mag} -dominated also in the denser regions (e.g. Begelman & Silk 2017, and references therein) and not only in the upper layers (e.g. Miller & Stone 2000), possibly solving a few long-standing issues of the standard accretions disk theory (Dexter & Begelman 2019). Simulations indeed showed that P_{mag} can become an important competitor in supporting the disk vertically (Bai & Stone 2013; Salvesen et al. 2016), although heavily depending on the strength of the net vertical magnetic field, the origin of which is not fully understood, yet. If this imposed net vertical field is small (if $\beta_0 = P_{\text{tot}}/P_{\text{mag}} \gg 1$), the buoyant escape of the toroidal component, amplified by MRI, is faster than its creation and a disk-corona system consistent with our model is formed. However, the evidence of disks that are magnetically-dominated even at the mid-plane is supported by Jiang et al. (2019), that recently performed a global 3D radiation-MHD simulation of two sub-Eddington flows. The structure of their simulated disks is significantly different from the standard SS73 model and reaches a complexity that our simplified prescriptions are not able to grasp. On the other hand, these simulations could not produce spectra and luminosities, yet. We here rely on the assumption that the energetics of P_{mag} -dominated disks are not significantly different from standard thin disks at radii larger than $\sim 10r_g$ (e.g., see Sdowski 2016).

6.2.3. Winds and outflows

In order to see if any known broad absorption line (BAL) quasars were present in our sample, we cross-matched the XMM-XXL catalog (L16; Menzel et al. 2016) with SDSS-DR12 (Pâris et al. 2017), that flagged 29580 BAL QSO after visual inspection.

Only two sources among the 379 used in our analysis were flagged, although they were both assigned zero indexes in the common metrics used for a more quantitative measurement of the BAL properties (Pâris et al. 2017). Hence, our sample has no contaminations from known BALs, although we can investigate the possible impact of un-modeled wind-dominated objects on our work. For instance, Nomura et al. (2018) recently developed a disk model compensating for the mass-loss rates of UV-driven winds, while consistently adjusting the temperature and emission of the underlying disk. They referred to a future work for a more complete modeling of the inner radii and the hard X-ray emission, but the influence on $L_{3000\text{\AA}}$ values seems already significant, provided $\dot{m} \gtrsim 0.5$. Since winds appear to act only from moderate to Eddington \dot{m} , neglecting their presence would have an impact on the modeled L_X-L_{UV} slope. The wind carries away kinetic energy reducing the disk emission accordingly, thus for a given observed high $L_{3000\text{\AA}}$, our no-wind model would underestimate \dot{m} for the possible outflowing sources contaminating our sample.

6.2.4. The larger-than-predicted disk argument

One of the most studied issues of the standard SS73 disk model is that observed sizes appear to be larger than expected at optical-UV wavelengths, using both microlensing effects (e.g. Morgan et al. 2010; Blackburne et al. 2011; Jiménez-Vicente et al. 2012) and flux variability lags across multiple bands in the so-called reprocessing scenario (e.g. Edelson et al. 2015; Fausnaugh et al. 2016, 2018; Jiang et al. 2017b; Cackett et al. 2018; McHardy et al. 2018), in which often a compact X-ray emitting region (e.g., a lamppost corona) irradiates the disk inducing light-travel lags in the UV-optical bands. However, even combining all these results discordant with the theoretical predictions is not trivial (Kokubo 2018), particularly if different techniques are used (see Moreno et al. 2018; Vio & Andreani 2018). What is more, there are also numerous studies finding consistency with the sizes predicted by the standard SS73 theory (e.g. McHardy et al. 2016; Mudd et al. 2018; Yu et al. 2018; Edelson et al. 2019; Homayouni et al. 2019), thus we do not consider necessary to use the larger-than-predicted argument to abandon all the standard prescriptions, yet.

6.2.5. No-torque inner boundary

For convenience, we adopted the no-torque condition with the stress vanishing at the inner edge. However, the presence of magnetic torques (Gammie 1999; Agol & Krolik 2000) would increase the disk effective temperature and the Q_+ emissivity in the innermost radii (Agol & Krolik 2000; Dezen & Flores 2018) and, if applied to the disk only, it would cause instead a drop in the fraction f (Merloni & Fabian 2003). Without a proper MHD treatment, it is unclear how the modeled $L_{2\text{keV}} \propto fQ_+$ would be affected, and consequently the L_X-L_{UV} slope.

6.2.6. The vertical structure

Our model does not properly treat the vertical structure of the disk. The effective temperature is obtained from $T_{\text{eff}} \propto T_{\text{mid}}/\tau^{1/4}$, where $\tau = h\rho\kappa$ assumes constant ρ and κ along the scale-height. Even keeping the approximation of a constant ρ , κ should change self-consistently with the decrease in temperature. A more thorough modeling of the disk vertical structure in supermassive

black holes was presented by Hubeny and collaborators, taking into account both scattering processes and free-free and bound-free opacities (Hubeny et al. 2000, 2001). Their model also share some of our limits (e.g., stationary disk, α -prescription, no-torque boundary, vertical support from thermal pressure only), validating the comparison. The overall SED has lower (higher) fluxes at low (high) frequencies with respect to standard calculations, with the most significant impact on the modeling of the soft-excess (Done et al. 2012). The computation of $L_{3000\text{\AA}}$ should be affected in a minor way, with a small overestimation on the order of a color correction (e.g. Done et al. 2012), that is either roughly constant or weakly depending on m and \dot{m} (e.g. Davis & El-Abd 2019). Our conclusions should not be significantly affected, although this would need to be improved for a proper SED modeling and time-lags predictions.

7. Conclusions

The gap between simulations and observations in AGN needs to be bridged and simplified, but motivated, analytic prescriptions still represent a powerful tool to explain the observed multi-wavelength scaling relations. For instance, the clear correlation observed between monochromatic logarithmic L_X and L_{UV} luminosities has been used for decades (in the shape of the more-known α_{OX} parameter, Tananbaum et al. 1979) in many applications (even for cosmology, e.g. Risaliti & Lusso 2015, 2019). Despite this, a conclusive theoretical explanation for the observed correlation is still lacking. Being smaller than one, the observed slope indicates that, going from low- to high-accretion rate AGN, the X-ray emission increases less than the optical-UV emission. Any viable disk-corona model must be able to explain this.

In this work, we tested a self-consistent disk-corona model (Sect. 2, see also M03) against the L_X-L_{UV} relation. We were able to identify the possible mechanism regulating the disk-corona energetic interplay, in terms of viscosity prescriptions (e.g., $\mu = 0.5$) that naturally lead to an X-ray emission increasing less than the disk emission going to higher accretion rates (see Sect. 3).

We also put forward a quantitative observational test (Sect. 4), using a reference sample of AGN (Sect. 4.1) observed both in the (rest-frame) UV and in X-rays: taking from each source the observationally determined m , \dot{m} and Γ we were able to model an analogous mock object (Sect. 4.2) producing a set of mock L_X-L_{UV} . This allowed us to reach a deep understanding of the physics driving the slope, normalization and scatter of the L_X-L_{UV} (see Sect. 5).

We find that if the black-hole population is assumed to be non-spinning, results from this test are inconclusive: the viscosity prescriptions reproducing the slope of the observed L_X-L_{UV} relation, also produce overly weak coronae. Interestingly enough, the tension between the strength of the observed and modeled X-ray emission (i.e. in the normalization of the L_X-L_{UV}) can be significantly relaxed adopting a more realistic high-spinning black-hole population and/or with moderately-outflowing coronae. We tested the former case adopting the efficiency (and the inner orbit) of maximally-spinning black holes, in which matter is able to accrete further into the potential well, resulting in a much higher accretion power and, consequently, in much stronger coronae (Sect. 5.6). Moreover, if the spin is high the X-ray emission profile peaks closer to the black hole, in even better agreement with X-ray reverberation and microlensing studies (Mosquera et al. 2013; Reis & Miller 2013; Wilkins et al. 2016). In particular, the disk-corona model

testing maximally-spinning black holes with $\mu = 0.5$ (i.e. magnetic stress proportional to the geometric mean of P_{gas} and P_{tot} , e.g. see M03), $f_{\text{max}} = 0.9$, $\alpha_0 = 0.02$ (see Table 1) provides the best match with the observations (Fig. 10), although the modeled slope is still somewhat larger than the observed one (Fig. 9). Going beyond this type of exercises, only 3D global radiation-MHD simulations will be able to better disclose the disk-corona physics (e.g. Jiang et al. 2017a, 2019), provided a clearer way of approaching the observations will be reached.

Acknowledgements. We thank the referee for his/her helpful comments. We thank Teng Liu for kindly providing the optical spectral slopes obtained in (Liu et al. 2018). We are also grateful to Torben Simm for the RM-QSO data and to Elisabeta Lusso and Guido Risaliti for making available to us the data of LR17. RA thanks Damien Coffey, Jacob Ider Chitham and Linda Baronchelli for insightful discussions. We acknowledge the use of the matplotlib package (Hunter 2007).

References

- Agol, E., & Krolik, J. H. 2000, *ApJ*, 528, 161
 Antonucci, R. 2015, ArXiv e-prints [arXiv:1501.02001]
 Bai, X.-N., & Stone, J. M. 2013, *ApJ*, 767, 30
 Balbus, S. A., & Hawley, J. F. 1991, *ApJ*, 376, 214
 Balbus, S. A., & Hawley, J. F. 1992, *ApJ*, 400, 610
 Baronchelli, L., Nandra, K., & Buchner, J. 2018, *MNRAS*, 480, 2377
 Begelman, M. C., & Silk, J. 2017, *MNRAS*, 464, 2311
 Beloborodov, A. M. 1999, in High Energy Processes in Accreting Black Holes, eds. J. Poutanen, & R. Svensson, *ASP Conf. Ser.*, 161, 295
 Beloborodov, A. M. 2017, *ApJ*, 850, 141
 Blackburne, J. A., Pooley, D., Rappaport, S., & Schechter, P. L. 2011, *ApJ*, 729, 34
 Blackman, E. G., & Pessah, M. E. 2009, *ApJ*, 704, L113
 Blaes, O. 2007, *ASP Conf. Ser.*, 373, 75
 Blaes, O. 2014, *Space Sci. Rev.*, 183, 21
 Blaes, O., & Socrates, A. 2001, *ApJ*, 553, 987
 Boissay, R., Ricci, C., & Paltani, S. 2016, *A&A*, 588, A70
 Brenneman, L. W., Reynolds, C. S., Nowak, M. A., et al. 2011, *ApJ*, 736, 103
 Buchner, J., Georgakakis, A., Nandra, K., et al. 2014, *A&A*, 564, A125
 Burm, H. 1985, *A&A*, 143, 389
 Cackett, E. M., Chiang, C.-Y., McHardy, I., et al. 2018, *ApJ*, 857, 53
 Cao, X. 2009, *MNRAS*, 394, 207
 Capellupo, D. M., Netzer, H., Lira, P., Trakhtenbrot, B., & Mejía-Restrepo, J. 2015, *MNRAS*, 446, 3427
 Capellupo, D. M., Netzer, H., Lira, P., Trakhtenbrot, B., & Mejía-Restrepo, J. 2016, *MNRAS*, 460, 212
 Chandrasekhar, S. 1960, *Proc. Natl. Acad. Sci.*, 46, 253
 Chiaraluca, E., Vagnetti, F., Tombesi, F., & Paolillo, M. 2018, *A&A*, 619, A95
 Crummy, J., Fabian, A. C., Gallo, L., & Ross, R. R. 2006, *MNRAS*, 365, 1067
 Czerny, B., Du, P., Wang, J.-M., & Karas, V. 2016, *ApJ*, 832, 15
 D'Agostini, G. 2003, *Bayesian Reasoning in Data Analysis: A Critical Introduction* (New Jersey, USA: World Scientific)
 D'Agostini, G. 2005, ArXiv e-prints [arXiv:physics/0511182]
 Davis, S. W., & El-Abd, S. 2019, *ApJ*, 874, 23
 Davis, S. W., & Laor, A. 2011, *ApJ*, 728, 98
 Della Ceca, R., Caccianiga, A., Severgnini, P., et al. 2008, *A&A*, 487, 119
 De Marco, B., Ponti, G., Cappi, M., et al. 2013, *MNRAS*, 431, 2441
 Dexter, J., & Begelman, M. C. 2019, *MNRAS*, 483, L17
 Dezen, T., & Flores, B. 2018, *ApJ*, 861, 18
 Di Matteo, T. 1998, *MNRAS*, 299, L15
 Done, C., Davis, S. W., Jin, C., Blaes, O., & Ward, M. 2012, *MNRAS*, 420, 1848
 Edelson, R., Gelbord, J. M., Horne, K., et al. 2015, *ApJ*, 806, 129
 Edelson, R., Gelbord, J., Cackett, E., et al. 2019, *ApJ*, 870, 123
 Elvis, M., Maccacaro, T., Wilson, A. S., et al. 1978, *MNRAS*, 183, 129
 Fabian, A. C., Zoghbi, A., Ross, R. R., et al. 2009, *Nature*, 459, 540
 Fabian, A. C., Alston, W. N., Cackett, E. M., et al. 2017, *Astron. Nachr.*, 338, 269
 Fausnaugh, M. M., Denney, K. D., Barth, A. J., et al. 2016, *ApJ*, 821, 56
 Fausnaugh, M. M., Starkey, D. A., Horne, K., et al. 2018, *ApJ*, 854, 107
 Foreman-Mackey, D., Hogg, D. W., Lang, D., & Goodman, J. 2013, *PASP*, 125, 306
 Galeev, A. A., Rosner, R., & Vaiana, G. S. 1979, *ApJ*, 229, 318
 Gammie, C. F. 1999, *ApJ*, 522, L57
 Garcia, J. A., Kara, E., Walton, D., et al. 2019, *ApJ*, 871, 88

- Grzędziński, M., Janiuk, A., Czerny, B., & Wu, Q. 2017a, *A&A*, **603**, A110
- Grzędziński, M., Janiuk, A., & Czerny, B. 2017b, *ApJ*, **845**, 20
- Haardt, F., & Maraschi, L. 1991, *ApJ*, **380**, L51
- Haardt, F., & Maraschi, L. 1993, *ApJ*, **413**, 507
- Haardt, F., Maraschi, L., & Ghisellini, G. 1994, *ApJ*, **432**, L95
- Hawley, J. F., & Balbus, S. A. 1991, *ApJ*, **376**, 223
- Hawley, J. F., & Balbus, S. A. 1992, *ApJ*, **400**, 595
- Hawley, J. F., Gammie, C. F., & Balbus, S. A. 1995, *ApJ*, **440**, 742
- Homayouni, Y., Trump, J. R., Grier, C. J., et al. 2019, *ApJ*, **880**, 126
- Hopkins, P. F., Richards, G. T., & Hernquist, L. 2007, *ApJ*, **654**, 731
- Hoshi, R. 1985, in *Galactic and Extra-Galactic Compact X-ray Sources*, eds. Y. Tabaka, & W. H. G. Lewin, 143
- Hubeny, I., Agol, E., Blaes, O., & Krolik, J. H. 2000, *ApJ*, **533**, 710
- Hubeny, I., Blaes, O., Krolik, J. H., & Agol, E. 2001, *ApJ*, **559**, 680
- Hunter, J. D. 2007, *Comput. Sci. Eng.*, **9**, 90
- Ichimaru, S. 1977, *ApJ*, **214**, 840
- Janiuk, A., Czerny, B., & Życki, P. T. 2000, *MNRAS*, **318**, 180
- Jansen, F., Lumb, D., Altieri, B., et al. 2001, *A&A*, **365**, L1
- Jiang, Y.-F., Stone, J. M., & Davis, S. W. 2014, *ApJ*, **784**, 169
- Jiang, Y.-F., Davis, S. W., & Stone, J. M. 2016, *ApJ*, **827**, 10
- Jiang, Y. F., Stone, J., & Davis, S. W. 2017a, ArXiv e-prints [arXiv:1709.02845]
- Jiang, Y.-F., Green, P. J., Greene, J. E., et al. 2017b, *ApJ*, **836**, 186
- Jiang, Y. F., Blaes, O., Stone, J., & Davis, S. W. 2019, *ApJ*, submitted [arXiv:1904.01674]
- Jiménez-Vicente, J., Mediavilla, E., Muñoz, J. A., & Kochanek, C. S. 2012, *ApJ*, **751**, 106
- Jin, C., Ward, M., & Done, C. 2012, *MNRAS*, **422**, 3268
- Kadowaki, L. H. S., de Gouveia Dal Pino, E. M., & Stone, J. M. 2018, *ApJ*, **864**, 52
- Kelly, B. C., Bechtold, J., Trump, J. R., Vestergaard, M., & Siemiginowska, A. 2008, *ApJS*, **176**, 355
- Kilerci Eser, E., & Vestergaard, M. 2018, *MNRAS*, **474**, 1590
- Kishimoto, M., Antonucci, R., Blaes, O., et al. 2008, *Nature*, **454**, 492
- Kokubo, M. 2018, *PASJ*, **70**, 97
- Koratkar, A., & Blaes, O. 1999, *PASP*, **111**, 1
- Krawczyk, C. M., Richards, G. T., Mehta, S. S., et al. 2013, *ApJS*, **206**, 4
- Kubota, A., & Done, C. 2018, *MNRAS*, **480**, 1247
- Liang, E. P. T., & Price, R. H. 1977, *ApJ*, **218**, 247
- Lightman, A. P., & Eardley, D. M. 1974, *ApJ*, **187**, L1
- Lightman, A. P., & White, T. R. 1988, *ApJ*, **335**, 57
- Liu, J.-Y., & Liu, B.-F. 2009, *Res. Astron. Astrophys.*, **9**, 966
- Liu, B. F., Mineshige, S., & Shibata, K. 2002, *ApJ*, **572**, L173
- Liu, J. Y., Liu, B. F., Qiao, E. L., & Mineshige, S. 2012, *ApJ*, **754**, 81
- Liu, J. Y., Qiao, E. L., & Liu, B. F. 2016a, *ApJ*, **833**, 35
- Liu, Z., Merloni, A., Georgakakis, A., et al. 2016b, *MNRAS*, **459**, 1602
- Liu, T., Merloni, A., Wang, J.-X., et al. 2018, *MNRAS*, **479**, 5022
- Lusso, E. 2019, *Astron. Nachr.*, **340**, 267
- Lusso, E., & Risaliti, G. 2016, *ApJ*, **819**, 154
- Lusso, E., & Risaliti, G. 2017, *A&A*, **602**, A79
- Lusso, E., Comastri, A., Vignali, C., et al. 2010, *A&A*, **512**, A34
- Lusso, E., Comastri, A., Simmons, B. D., et al. 2012, *MNRAS*, **425**, 623
- Malzac, J., Beloborodov, A. M., & Poutanen, J. 2001, *MNRAS*, **326**, 417
- Marconi, A., Risaliti, G., Gilli, R., et al. 2004, *MNRAS*, **351**, 169
- McHardy, I. M. 1989, in *Two Topics in X-Ray Astronomy, Volume 1: X Ray Binaries. Volume 2: AGN and the X Ray Background*, eds. J. Hunt, & B. Battrick, *ESA Spec. Publ.*, 296
- McHardy, I. M., Connolly, S. D., Peterson, B. M., et al. 2016, *Astron. Nachr.*, **337**, 500
- McHardy, I. M., Connolly, S. D., Horne, K., et al. 2018, *MNRAS*, **480**, 2881
- Menzel, M.-L., Merloni, A., Georgakakis, A., et al. 2016, *MNRAS*, **457**, 110
- Merloni, A. 2003, *MNRAS*, **341**, 1051
- Merloni, A., & Fabian, A. C. 2002, *MNRAS*, **332**, 165
- Merloni, A., & Fabian, A. C. 2003, *MNRAS*, **342**, 951
- Merloni, A., & Nayakshin, S. 2006, *MNRAS*, **372**, 728
- Merloni, A., Malzac, J., Fabian, A. C., & Ross, R. R. 2006, *MNRAS*, **370**, 1699
- Merloni, A., Bongiorno, A., Brusa, M., et al. 2014, *MNRAS*, **437**, 3550
- Meyer, F., & Meyer-Hofmeister, E. 1982, *A&A*, **106**, 34
- Middei, R., Bianchi, S., Petrucci, P.-O., et al. 2019, *MNRAS*, **483**, 4695
- Miller, K. A., & Stone, J. M. 2000, *ApJ*, **534**, 398
- Minoshima, T., Hirose, S., & Sano, T. 2015, *ApJ*, **808**, 54
- Moreno, J., Vogeley, M. S., & Richards, G. T. 2018, *PASP*, submitted [arXiv:1811.00154]
- Morgan, C. W., Kochanek, C. S., Morgan, N. D., & Falco, E. E. 2010, *ApJ*, **712**, 1129
- Mosquera, A. M., Kochanek, C. S., Chen, B., et al. 2013, *ApJ*, **769**, 53
- Mudd, D., Martini, P., Zu, Y., et al. 2018, *ApJ*, **862**, 123
- Nandra, K., Pounds, K. A., Stewart, G. C., et al. 1991, *MNRAS*, **248**, 760
- Nandra, K., O'Neill, P. M., George, I. M., & Reeves, J. N. 2007, *MNRAS*, **382**, 194
- Nomura, M., Ohsuga, K., & Done, C. 2018, *MNRAS*, submitted [arXiv:1811.01966]
- Pâris, I., Petitjean, P., Ross, N. P., et al. 2017, *A&A*, **597**, A79
- Petrucci, P.-O., Ursini, F., De Rosa, A., et al. 2018, *A&A*, **611**, A59
- Pierre, M., Pacaud, F., Adami, C., et al. 2016, *A&A*, **592**, A1
- Pounds, K. A., Nandra, K., Stewart, G. C., George, I. M., & Fabian, A. C. 1990, *Nature*, **344**, 132
- Pringle, J. E. 1976, *MNRAS*, **177**, 65
- Pringle, J. E. 1981, *ARA&A*, **19**, 137
- Reis, R. C., & Miller, J. M. 2013, *ApJ*, **769**, L7
- Reynolds, C. S. 2013, *Classical and Quantum Gravity*, **30**, 244004
- Reynolds, C. S. 2019, *Nat. Astron.*, **3**, 41
- Richards, G. T., Lacy, M., Storrie-Lombardi, L. J., et al. 2006, *ApJS*, **166**, 470
- Ripperda, B., Porth, O., Sironi, L., & Keppens, R. 2019, *MNRAS*, **485**, 299
- Risaliti, G., & Lusso, E. 2015, *ApJ*, **815**, 33
- Risaliti, G., & Lusso, E. 2019, *Nat. Astron.*, **3**, 272
- Ross, J., Latter, H. N., & Guilet, J. 2016, *MNRAS*, **455**, 526
- Runnoe, J. C., Brotherton, M. S., & Shang, Z. 2012, *MNRAS*, **422**, 478
- Sakimoto, P. J., & Coroniti, F. V. 1981, *ApJ*, **247**, 19
- Salvesen, G., Simon, J. B., Armitage, P. J., & Begelman, M. C. 2016, *MNRAS*, **457**, 857
- Sano, T., Inutsuka, S.-I., Turner, N. J., & Stone, J. M. 2004, *ApJ*, **605**, 321
- Sdowski, A. 2016, *MNRAS*, **459**, 4397
- Schnittman, J. D., Krolik, J. H., & Noble, S. C. 2013, *ApJ*, **769**, 156
- Seaton, M. J. 1995, *The Opacity Project* (Bristol, UK: Institute of Physics Pub.)
- Seaton, M. J., Yan, Y., Mihalas, D., & Pradhan, A. K. 1994, *MNRAS*, **266**, 805
- Shadmehri, M., Khajenabi, F., Dib, S., & Inutsuka, S.-I. 2018, *MNRAS*, **481**, 5170
- Shakura, N. I., & Sunyaev, R. A. 1973, *A&A*, **24**, 337
- Shakura, N. I., & Sunyaev, R. A. 1976, *MNRAS*, **175**, 613
- Shapiro, S. L. 2005, *ApJ*, **620**, 59
- Shen, Y. 2013, *Bull. Astron. Soc. India*, **41**, 61
- Shen, Y., & Liu, X. 2012, *ApJ*, **753**, 125
- Shen, Y., Greene, J. E., Strauss, M. A., Richards, G. T., & Schneider, D. P. 2008, *ApJ*, **680**, 169
- Shen, Y., Hall, P. B., Horne, K., et al. 2019, *ApJS*, **241**, 34
- Slone, O., & Netzer, H. 2012, *MNRAS*, **426**, 656
- Steffen, A. T., Strateva, I., Brandt, W. N., et al. 2006, *AJ*, **131**, 2826
- Stella, L., & Rosner, R. 1984, *ApJ*, **277**, 312
- Stern, B. E., Poutanen, J., Svensson, R., Sikora, M., & Begelman, M. C. 1995, *ApJ*, **449**, L13
- Strateva, I. V., Brandt, W. N., Schneider, D. P., Vanden Berk, D. G., & Vignali, C. 2005, *AJ*, **130**, 387
- Strüder, L., Briel, U., Dennerl, K., et al. 2001, *A&A*, **365**, L18
- Svensson, R., & Zdziarski, A. A. 1994, *ApJ*, **436**, 599
- Szuskiewicz, E. 1990, *MNRAS*, **244**, 377
- Taam, R. E., & Lin, D. N. C. 1984, *ApJ*, **287**, 761
- Tanaka, Y., Nandra, K., Fabian, A. C., et al. 1995, *Nature*, **375**, 659
- Tananbaum, H., Avni, Y., Branduardi, G., et al. 1979, *ApJ*, **234**, L9
- Thorne, K. S. 1974, *ApJ*, **191**, 507
- Turner, T. J., & Pounds, K. A. 1989, *MNRAS*, **240**, 833
- Turner, M. J. L., Abbey, A., Arnaud, M., et al. 2001, *A&A*, **365**, L27
- Turner, N. J., Stone, J. M., & Sano, T. 2002, *ApJ*, **566**, 148
- Uttler, P., Cackett, E. M., Fabian, A. C., Kara, E., & Wilkins, D. R. 2014, *A&ARv*, **22**, 72
- Uzdensky, D. A. 2013, *ApJ*, **775**, 103
- Uzdensky, D. A. 2016, *Astrophys. Space Sci. Lib.*, **427**, 473
- Uzdensky, D. A., & Goodman, J. 2008, *ApJ*, **682**, 608
- Vagnetti, F., Antonucci, M., & Trevese, D. 2013, *A&A*, **550**, A71
- Vasudevan, R. V., & Fabian, A. C. 2007, *MNRAS*, **381**, 1235
- Vasudevan, R. V., & Fabian, A. C. 2009, *MNRAS*, **392**, 1124
- Vasudevan, R. V., Fabian, A. C., Reynolds, C. S., et al. 2016, *MNRAS*, **458**, 2012
- Vignali, C., Brandt, W. N., & Schneider, D. P. 2003, *AJ*, **125**, 433
- Vio, R., & Andreani, P. 2018, ArXiv e-prints [arXiv:1812.03995]
- Wang, J.-M., Watarai, K.-Y., & Mineshige, S. 2004, *ApJ*, **607**, L107
- Wang, C., Yu, L.-M., Bian, W.-H., & Zhao, B.-X. 2019, *MNRAS*, **487**, 2463
- Werner, G. R., Philippov, A. A., & Uzdensky, D. A. 2019, *MNRAS*, **482**, L60
- Wilkins, D. R., Cackett, E. M., Fabian, A. C., & Reynolds, C. S. 2016, *MNRAS*, **458**, 200
- Williams, O. R., Turner, M. J. L., Stewart, G. C., et al. 1992, *ApJ*, **389**, 157
- You, B., Cao, X., & Yuan, Y.-F. 2012, *ApJ*, **761**, 109
- Young, M., Elvis, M., & Risaliti, G. 2009, *ApJS*, **183**, 17
- Young, M., Elvis, M., & Risaliti, G. 2010, *ApJ*, **708**, 1388
- Yu, Z., Martini, P., Davis, T. M., et al. 2018, ArXiv e-prints [arXiv:1811.03638]

Appendix A: Disc-corona equations

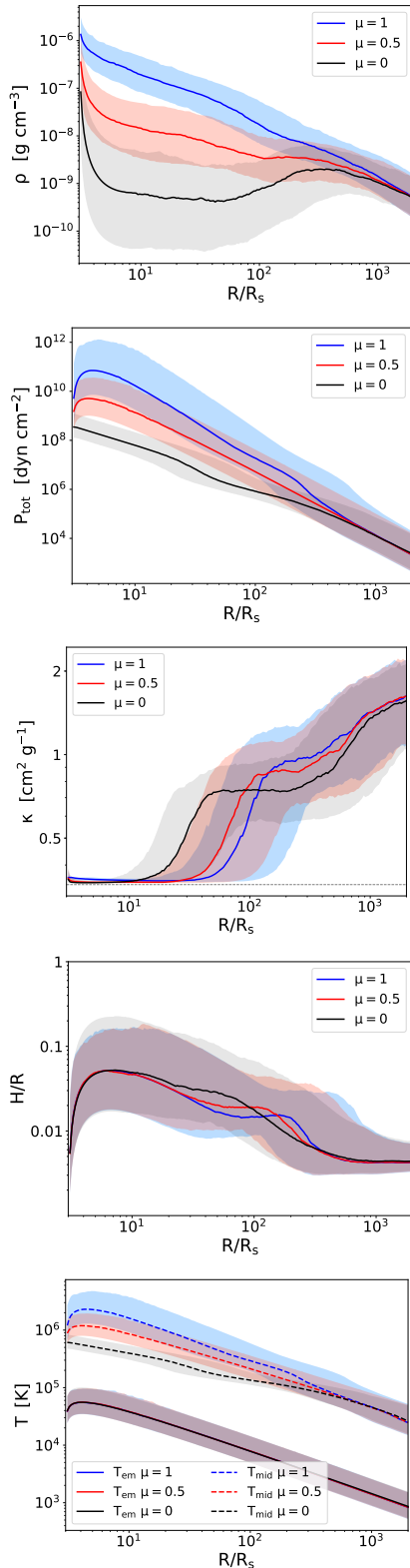


Fig. A.1. Same as Fig. 1, with radial profiles for the mid-plane ρ (top left), P_{tot} (gas plus radiation, top central), κ (top right), h/r (bottom left) and T (both mid-plane and surface, bottom right).

We report the equations for h , mid-plane ρ (g cm^{-3}), P (dyn cm^{-2}), T (K, at the mid-plane) and the closure equation for

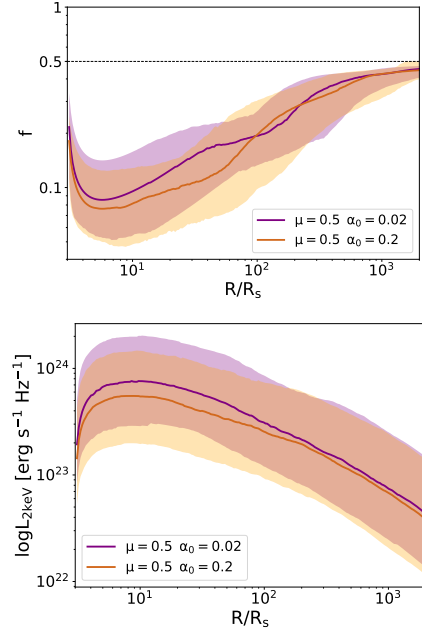


Fig. A.2. Same as in Figs. 1 and A.1. Here, we highlight the (minor) influence on varying α_0 from 0.02 (purple) to 0.2 (orange) in f - and $L_{2\text{keV}}$ -profiles.

f . In the radiation pressure dominated regime:

$$\begin{aligned} \rho &= \rho_{\text{const}} k_0^{-\frac{4}{\mu+4}} [\alpha_0 m]^{-\frac{4}{\mu+4}} [\dot{m}J(r)]^{\frac{2(3\mu-4)}{\mu+4}} r^{\frac{3(2-3\mu)}{\mu+4}} (1-\tilde{f})^{\frac{6(\mu-2)}{\mu+4}} \\ T &= T_{\text{const}} k_0^{-\frac{1}{\mu+4}} [\alpha_0 m]^{-\frac{1}{\mu+4}} [\dot{m}J(r)]^{\frac{2\mu}{\mu+4}} r^{\frac{3(2\mu^2-3\mu-2)}{2(2-\mu)(\mu+4)}} (1-\tilde{f})^{\frac{2\mu-1}{\mu+4}} \\ h &= 9.14 \dot{m}J(r)(1-\tilde{f}) \\ P &= P_{\text{const}} k_0^{-\frac{4}{\mu+4}} [\alpha_0 m]^{-\frac{4}{\mu+4}} [\dot{m}J(r)]^{\frac{8\mu}{\mu+4}} r^{\frac{6(2\mu^2-3\mu-2)}{(2-\mu)(\mu+4)}} (1-\tilde{f})^{\frac{4(2\mu-1)}{\mu+4}} \\ \frac{(2\alpha_0)^{1/\mu} - k_1^{2/\mu} f^{2/\mu}}{k_1^{2/\mu} f^{2/\mu}} &= \tilde{C} k_0^{\frac{1}{\mu+4}} [\alpha_0 m]^{\frac{1}{\mu+4}} [\dot{m}J(r)]^{\frac{8}{\mu+4}} r^{-\frac{21}{2(\mu+4)}} (1-\tilde{f})^{\frac{9}{\mu+4}} \end{aligned} \quad (\text{A.1})$$

where k_0 is the proportionality constant between the stress tensor and the magnetic pressure. The constant values depend on μ as follows:

$$\begin{aligned} \rho_{\text{const}} &= (4.7 \times 10^{-68})^{\frac{6(2-\mu)}{\mu+4}} (5.5 \times 10^{48})^{\frac{2(8-3\mu)}{\mu+4}} (1.5 \times 10^{-23})^{\frac{4\mu}{\mu+4}} \\ T_{\text{const}} &= (4.7 \times 10^{-68})^{\frac{1-2\mu}{\mu+4}} (5.5 \times 10^{48})^{\frac{2(\mu^2-3\mu+2)}{(2-\mu)(\mu+4)}} (1.5 \times 10^{-23})^{\frac{\mu}{\mu+4}} \\ P_{\text{const}} &= \frac{a}{3} (4.7 \times 10^{-68})^{\frac{4(1-2\mu)}{\mu+4}} (5.5 \times 10^{48})^{\frac{8(\mu^2-3\mu+2)}{(2-\mu)(\mu+4)}} (1.5 \times 10^{-23})^{\frac{4\mu}{\mu+4}} \\ \tilde{C} &= (4.7 \times 10^{-68})^{\frac{-9}{\mu+4}} (5.5 \times 10^{48})^{\frac{-10}{\mu+4}} (1.5 \times 10^{-23})^{\frac{4}{\mu+4}}. \end{aligned} \quad (\text{A.2})$$

The solutions for gas pressure dominated regions, that are independent on the choice of μ in the viscosity law, are:

$$\begin{aligned} \rho &= 14.44 k_0^{-3/5} \xi^{3/10} [\alpha_0 m]^{-7/10} [\dot{m}J(r)]^{2/5} r^{-33/20} (1-\tilde{f})^{-3/10} \\ T &= 8.01 \times 10^8 k_0^{-4/15} \xi^{-1/5} [\alpha_0 m]^{-1/5} [\dot{m}J(r)]^{2/5} r^{-9/10} (1-\tilde{f})^{1/5} \\ h &= 1.72 \times 10^{-2} k_0^{-7/15} \xi^{-1/10} [\alpha_0 m]^{-1/10} [\dot{m}J(r)]^{1/5} r^{21/20} (1-\tilde{f})^{1/10} \\ P &= 1.91 \times 10^8 k_0^{-13/15} \xi^{1/10} [\alpha_0 m]^{-9/10} [\dot{m}J(r)]^{4/5} r^{-51/20} (1-\tilde{f})^{-1/10} \\ \frac{4\alpha_0^2 - k_1^4 f^4}{k_1^4 f^4} &= 5.41 \times 10^2 k_0^{-1/5} \xi^{-9/10} [\alpha_0 m]^{1/10} [\dot{m}J(r)]^{4/5} r^{-21/20} (1-\tilde{f})^{9/10}. \end{aligned} \quad (\text{A.3})$$

The value of ξ can be obtained by studying the continuity of all the above quantities at the boundary between the radiation pressure- to the gas pressure-dominated regions. It corresponds to $\xi \simeq 1.00k_0^{-1/3}$.

In Fig. A.1 we report examples of radial profiles for ρ , P_{tot} , κ , h/r , T_{mid} and T_{eff} . Similar examples for f and $L_{2\text{keV}}$ are shown in Fig. 1. Once f_{max} is fixed, the dominant variance among the models is given by the choice of the viscosity law (μ), while α_0 plays a minor role. This is shown in Fig. A.2, where profiles for f and $L_{2\text{keV}}$ show little difference in varying α_0 from 0.02 to 0.2.

Appendix B: The reference AGN sample

For the source-by-source modeling of XMM-XXL we used the 379 sources obtained following the methodology outlined in Sect. 4.2. In Fig. B.1 we show the distribution of $L_{2\text{keV}}$ (top panel) and $L_{3000\text{\AA}}$ (bottom panel) in the luminosity-redshift plane of the 379 sources of our XMM-XXL sample (red and blue respectively), with respect to the parent sample of BLAGN from L16 (black). The L_X-L_{UV} slope of this reference sample is 0.54 ± 0.02 , from Eq. (12). This is incompatibly flatter than the values quoted in the recent literature, namely 0.64 ± 0.02 (Lusso & Risaliti 2016) or 0.63 ± 0.02 (LR17). The cleaning criteria applied in Sect. 4.1 were aimed to exclude low-quality data and to be consistent with the model, while in the above-mentioned literature the possible biases of flux-limited samples were treated carefully in order to reliably use quasars for cosmology (Risaliti & Lusso 2019).

We investigated whether this inconsistency in the slope would be bridged restricting the analysis to the brightest objects at all redshifts with a very crude and conservative selection. From the sensitivity curve of the XXL-N survey in the 0.5–10 keV band at half of the survey area (L16, their Fig. 3) we obtained the flux limit in that energy band. Then, we interpolated the flux limit at 2 keV using the mean photon index of the sample, obtaining the sensitivity curve shown in red in the top panel of Fig. B.1. In Menzel et al. (2016) a cut at $r < 22.5$ mag was applied. We converted this magnitude limit in a luminosity sensitivity only within $0.80 \lesssim z \lesssim 1.27$, for which 3000\AA was actually detected in the r band. For different redshifts, we first computed a redshift dependent color correction for the other bands (u , g , i and z) performing a linear regression on the difference with the r -band magnitude. This provided a magnitude limit for $L_{3000\text{\AA}}$ at all redshifts, consistently with the band in which that wavelength was actually detected, from which we obtained the related sensitivity line in the bottom panel of Fig. B.1. We then divided XMM-XXL in six redshift bins, making sure to have at least 30 counts per bin. For each bin, we excluded all the sources below the limits given by the sensitivity curves on both axis, evaluated at the maximum z of the bin to be conservative (Fig. B.2). The resulting cleanest subsample reaches accordance with the recent literature of the L_X-L_{UV} , with a slope of 0.59 ± 0.03 .

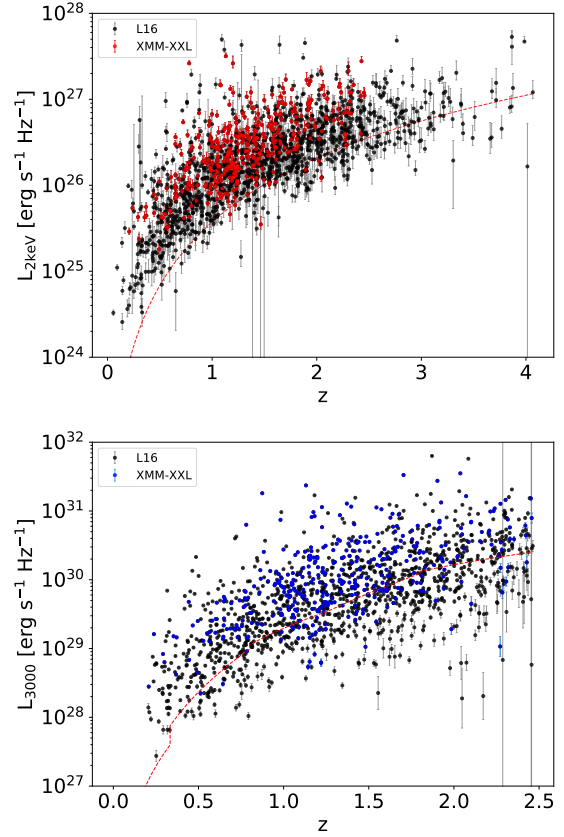


Fig. B.1. Distribution of $L_{2\text{keV}}$ (top panel) and $L_{3000\text{\AA}}$ (bottom panel) in the luminosity-redshift plane of the 379 sources of our XMM-XXL sample (red and blue respectively), with respect to the parent sample of BLAGN from L16 (black). The dashed red lines broadly represent the sensitivity of the survey at the related frequency (see the text for a description).

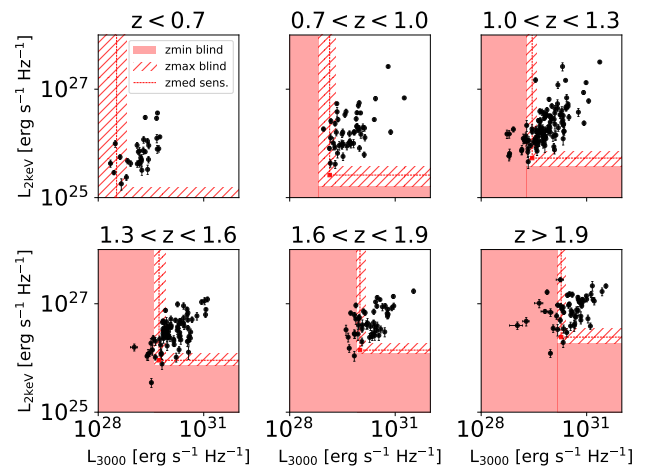


Fig. B.2. L_X-L_{UV} relation in the redshift bins reported in the sub-titles. The sensitivity surfaces at the minimum, median and maximum redshift of the bin are represented in red with a full area, a dashed line and a shaded area respectively. These surfaces are obtained from the sensitivity lines in Fig. B.1 at the above-mentioned redshifts. The sources above the shaded sensitivity area in each z -bin give the cleanest XMM-XXL sample.